Insight into Excitation and Acquisition Mechanism and Mode Control of Lamb Waves with Piezopolymer Coating-based Array Transducers: Analytical and Experimental Analysis

Yehai LI[a,b], Kai WANG[c], Wei FENG[b,d], Hefeng WU[a], Zhongqing SU[e] and Shifeng GUO[a,b,d,*]

[a]Shenzhen Key Laboratory of Smart Sensing and Intelligent Systems

Shenzhen Institute of Advanced Technology, Chinese Academy of Sciences, Shenzhen 518055,

P.R. China

[b]Guangdong Provincial Key Lab of Robotics and Intelligent System

Shenzhen Institute of Advanced Technology, Chinese Academy of Sciences, Shenzhen 518055,

P.R. China

[c]School of Aerospace Engineering

Xiamen University, Xiamen 361005, P.R. China

[d]University of Chinese Academy of Sciences, Beijing 10049, P.R. China

[e]Department of Mechanical Engineering

The Hong Kong Polytechnic University, Hung Hom, Kowloon 999077, Hong Kong SAR

* To whom correspondence should be addressed. Email: sf.guo@siat.ac.cn

Abstract

In-situ fabricated piezopolymer coating-based transducers have been developed to build large-area, lightweight and flexible networks for wave-based structural health monitoring (SHM). Meanwhile, their tunability can be realized by array electrodes for mode control with proper tuning methods. However, conventional *standard tuning* by phase matching seems not always effective. In this study, the excitation and acquisition mechanism of Piezopolymer Coating-based Array Transducers (PCATs) were first studied for Lamb waves. Distinctly different coupling mechanisms of PCAT actuators and sensors were discussed by analytical models and experimental verification, respectively. Then comprehensive parameter studies were performed to understand the filtering effect with finite temporal pulse duration of PCAT actuators, and finite spatial electrode span of PCAT actuators and sensors. Corresponding *bias tuning* methods were proposed with analytical solutions to improve mode control in Lamb-wave excitation and acquisition. This new guideline of designing array electrodes for PCAT actuators and sensors has been proven effective by successfully tuning the poor mode-controlled wavefield originated by the *standard tuning* method. Such tunability has great potential to be applied for detecting various damages in Lamb wave-based SHM, where sensitivity, accuracy, and signal interpretation can be improved with good control of particular frequency-mode selections.

1. Introduction

Lamb wave is a powerful tool to interrogate thin-walled engineering structures for structural health monitoring (SHM) with advantages as long-distance propagation, high sensitivity to damages, less attenuation, convenience to generate and detect, *etc*. However, the multi-mode and dispersive nature of Lamb waves make the signal complex for analysis. Moreover, different SHM applications usually favor particular frequency-mode selections, which would be more sensitive than others when interacting with certain types of damages. One typical family is single-mode excitation and acquisition, *e.g.* symmetric modes for through-thickness crack, antisymmetric modes for in-plane delamination [1]. Another family is different mode-to-mode selections for excitation and acquisition respectively, *e.g.* synchronous pair of modes for nonlinear measurement [2, 3], mode conversion under thickness variation [4] or scattered by damages[5]. Others include high-order modes cluster for high spatial and temporal resolution characteristics [6]. Thus, mode control is important to damage identification through achieving interpretable signals with strong desired modes and suppressed others.

To utilize the tunability of transducers for mode control in Lamb-wave excitation and acquisition, their fundamental coupling mechanism with attached structures is the priority to understand. The conventional Lamb-wave transducers can be categorized into displacement and strain types, and mostly share the same coupling mechanism in excitation and acquisition. Bulky ultrasonic transducers and laser vibrometers [7] for non-destructive evaluation are usually displacement-type transducers, due to their weakly coupling through agent like gel, water, or air which cannot effectively transfer shear traction. Displacement-type transducers excite Lamb waves through surface "tapping" structures (normal pressure over contact area) and capture Lamb waves by their normal displacement. The mode either

3

excited or detected can be controlled by Snell's law via angled wedges [8] or by constructive/destructive interference via time delay of phased array [9, 10]. Surface-mounted *in-situ* transducers for SHM, such as lead zirconate titanate wafers (PZTs) [11, 12] and macro-fiber composites (MFCs) [13], are generally treated as strain-type transducers, due to their firmly coupling through adhesive bonding and traction-free up-surface. They excite Lamb waves through surface "pinching" structures (shear stress at the edge of actuators under the ideal bonding condition) and sense Lamb waves by their in-plane strain. Giurgiutiu [14] has done comprehensive work on the coupling mechanism of PZTs and mode tuning by their dimensions and bonding quality through theoretical and experimental studies. The pin-force model was proposed as an effective assumption for generating Lamb waves by PZTs. For detecting Lamb waves, researchers tended to consider the same coupling model and tuning methods according to basic reciprocity principles. However, some work [15-17] indicated that the pin-force model and tuning behaviors for PZT actuators were not suitable for PZT sensors, while the response of PZTs to Lamb waves was actually governed by spatial averaging of the wavefield over the sensor-covered area. In SHM, it is always a challenge to control modes through the dimensions of a single PZT. Thus, different techniques have been developed for improving mode tunability. For example, a pair of surface-bonded PZTs on opposite sides were operated in-phase or out-of-phase for exciting and detecting either symmetric mode or antisymmetric mode [18]. Multiple PZTs were arrayed in either comb or inter-digital shape and mode control could be achieved by phase matching through changing pitch or adjusting time delay [19-21]. MFCs can be treated as arrayed rectangular PZTs with fixed pitch and control modes by time delay or tunable electrodes layout [13]. However, the fragility and limited life cycle of piezoceramic-based transducers like PZTs make them vulnerable to failure in industrial applications. Moreover, mode control via array transducers has a series of drawbacks that are detrimental to their practicability. Most concerns are

related to the finite thickness and the high stiffness of transducers, which may change the local waveguide and cause trouble for effective mode control [20]. The passing wavefield would be altered with dense-arrayed transducers [22]. Such disruption could complicate the acquired signals and confuse the damage-changed features. Furthermore, phased array technology by time delay requires complex electronics. Thus, the development of novel types of *in-situ* transducers may improve the performance of SHM on real structures with better flexibility and tunability. Those existing knowledge of conventional transducers could provide a good basis for investigating analytical models and design principles of novel transducers.

Flexible piezopolymer-based transducers are not brittle and can be applied on curved structures [23]. Polyvinylidene fluoride (PVDF) is the most widely investigated piezopolymer for SHM applications [24-27]. Conventional PVDF transducers are fabricated in the form of standalone thin films or membranes. Several functionalization procedures including phase transformation and polarization are required before being installed on structures by adhesive bonding. The electrodes can be easily printed on PVDF with customized shapes which makes it a perfect substrate to build array transducers with less worry about the influence of stiffness and thickness. Nevertheless, good mode control cannot be achieved without understanding the coupling mechanism. In some reported work, PVDF transducers were treated as strain coupling as PZTs due to the similar surface-mounted way by adhesive bonding on the structures [19, 28, 29]. Thus they share similar analytical models in exciting and detecting lamb waves and also similar tuning behaviors. On the other hand, there is also plenty of work that considered displacement coupling with PVDF transducers [30, 31]. The basic argument is that PVDF transducers are weakly coupled with metal structures due to low impedance and stiffness. To the best of the authors' knowledge, there

still lacks solid experimental verifications to solve such divergence.

With the development of intelligent manufacturing technology, 3D printing, or additive manufacturing, has been utilized for highly automated and rapid-prototyping fabrication of piezopolymer-based transducers [32-34]. In the authors' previous work [22], piezopolymer coatings were *in-situ* sprayed and functionalized directly on host structures. With proper printed electrodes and circuits, Piezopolymer Coating-based Array Transducers (PCATs) can be formed on a large scale and at high density with minimal weight/volume penalty to the host structure. The adhesive-free feature can further improve practicability by replacing conventional human installation. Despite the differences in manufacturing, PCATs work similarly to PVDF since both belong to piezopolymer-based transducers, and also lack an understanding of the coupling mechanism. Therefore, only basic constructive interference or phase matching was considered when designing electrode arrays for guided-wave excitation and acquisition. Matching the element pitch with the wavelength and element length with half the wavelength of the desired mode-frequency wave (*standard tuning* method) could achieve poor single-mode controlling in some cases [22]. Moreover, in many reported works, researchers applied the same *standard tuning* method for both Lamb-wave excitation and acquisition with piezopolymer-based transducers, either PVDF or PCAT, lacking further discussion on the possible nonconformity of coupling mechanisms and tuning methods of actuators and sensors.

To further exploit the capability of PCATs in Lamb wave-based SHM, in this study, the coupling mechanisms between PCATs and host structure for Lamb-wave excitation and acquisition are firstly investigated by analytical and experimental analysis. For Lamb-wave excitation, the excitability and source distribution are discussed by their influence on the

excited wavefield. Parameter studies considering the effects of the finite duration of the exciting pulse and finite dimensions of actuators are performed to discuss tunability. For Lamb-wave acquisition, the spatial averaging effect and wavenumber filtering of finite-dimension sensors are discussed in response to arbitrary and PCAT-excited wavefield. The acquisition mechanism of sensors is found to be distinctly different from the excitation mechanism of actuators by PCAT and so is the tuning behavior. Corresponding *bias tuning* methods have been proposed for mode control in Lamb-wave excitation and acquisition. This study provides an insight into the working mechanism and tunability of PCATs, which have shown a great potential for SHM applications. Meanwhile, these results could become a useful design tool for diverse damage identification with PCAT-based networks.

2. Lamb-wave Excitation by PCAT Actuators

The theory of Lamb wave should be recalled first. The free plate problem for isotropic materials with a thickness of *2d* can be derived as the dispersion equation:

$$\frac{\tan qd}{\tan pd} = -\left[\frac{4k^2 pq}{\left(q^2 - k^2\right)^2}\right]^{\pm 1},$$ **(1)**

where

$$p^2 = \frac{\omega^2}{C_L^2} - k^2, q^2 = \frac{\omega^2}{C_S^2} - k^2.$$

The exponent +1 is for symmetric and -1 for antisymmetric modes. ω is the circular frequency and frequency *f* equals $\omega/2\pi$. C_L and C_S are the longitudinal and shear wave velocities, respectively. *k* is the eigenvalue which can be solved numerically as $\xi_{S_0}, \xi_{S_1}, \xi_{S_2}\ldots$ and $\xi_{A_0}, \xi_{A_1}, \xi_{A_2}\ldots$, corresponding to wavenumbers of the symmetric modes and antisymmetric modes. The wavelength λ equals $2\pi/k$. For a given ω and derived *k*, the wave structures of displacement and stress across the thickness can be calculated (see **Equation**

A.1 in Appendix). The phase velocity C_p equals ω/k and the group velocity C_g equals $d\omega/dk$.

2.1. Analytical model

The analytical model is firstly established by decoupling the PCAT actuator and the attached waveguide (**Figure 1**). PCATs as described in authors' previous work [22] have at least two layers. The piezopolymer coatings are the function layer between the top and bottom electrode layers. If the structure is intrinsically conductive like metals, it can be used as the bottom layer directly. The excitation voltage *V(t)* is applied between the top and bottom layers and introduces electric fields on the function layer. Since the excitation mechanism is yet to be determined, both normal pressure *P(x)* of displacement coupling and shear stress *T(x)* of strain coupling are considered to be the excitation loads transferred on waveguide from PCAT actuators, with $x \in [0, x_0]$, where x_0 is the range of covered electrode layer.
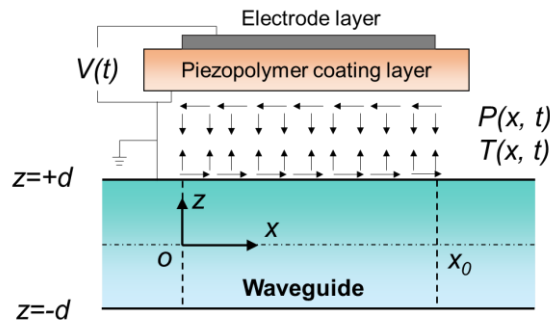

Figure 1. Analytical model of PCAT actuator on a metal waveguide.

PCAT has unique characteristics which are different from PZT and MFC:

a. The stiffness of PCAT is much lower than of the aluminum plate as host structure in this study;

b. The thickness of PCAT is ~20 μm, which is insignificant compared to the thickness of the host structure (2 mm in this study);

c. There is no adhesive layer between the piezopolymer coating layer and host structure;

8

d. PCAT has less interference in wave propagation than PZT [22].

Therefore, several assumptions are made to simplify the analytical model:

1. The strain is uniform along the thickness of PCAT;

2. The interaction between PCAT and host structure is considered as the ideal bonding condition, under which the pin-force model at the edge of actuators could be used for shear stress excitation;

3. Only the electrode-covered area of the function layer contributes to the excitation force;

4. PCAT is a non-resonant device, *i.e.,* the piezoelectric response not varying by frequency;

5. PCAT on host structure would not change the local waveguide and the passing wavefield;

6. The width of PCAT is infinite to ensure plane strain condition ($\partial/\partial y$=0) with straight-crested waves.

2.1.1 Excitability

To derive the excited wavefield by arbitrary loads, **Multiple Integral Transform Method** (MIT) and **Normal Mode Expansion Method** (NME) can be used as documented by textbooks [14, 35]. Since only surface-mounted actuators and sensors are discussed in this study, the wavefields (strain, stress, displacement) hereafter in this work refer to only surface components, *i.e.* under the condition of *z=d*, if not specified. Using MIT, the excited wavefield in the wavenumber-frequency (*k-ω*) domain can be described as

$$\bar{\bar{\boldsymbol{\varepsilon}}}(k,\omega) = \mathbf{N}_{\varepsilon}(k,\omega)\bar{\bar{\mathbf{F}}}(k,\omega)$$
$$\bar{\bar{\mathbf{u}}}(k,\omega) = \frac{1}{ik}\bar{\bar{\boldsymbol{\varepsilon}}}(k,\omega) = \mathbf{N}_{u}(k,\omega)\bar{\bar{\mathbf{F}}}(k,\omega)$$

, (2)

where $\bar{\bar{\boldsymbol{\varepsilon}}} = \begin{bmatrix} \bar{\bar{\varepsilon}}_{xx} & \bar{\bar{\varepsilon}}_{zz} \end{bmatrix}^{T}$ and $\bar{\bar{\mathbf{u}}} = \begin{bmatrix} \bar{\bar{u}}_{x} & \bar{\bar{u}}_{z} \end{bmatrix}^{T}$ are the excited strain and displacement

wavefields respectively. $\overline{\widetilde{\mathbf{F}}} = \begin{bmatrix} \overline{\widetilde{P}} & \overline{\widetilde{T}} \end{bmatrix}^T$ is the load function of excitation force. The bold letter indicates that the term is a vector or matrix. Operators - and ~ denote Fourier time and spatial transforms, respectively. $\mathbf{N}$ represents the excitability function of surface wavefields in the $k\text{-}\omega$ domain, which comprises four components related to different strain or displacement components under normal pressure and shear stress excitation due to the orthogonality (see also **Equation A.2** in Appendix):

$$\mathbf{N}_\varepsilon(k,\omega) = \begin{bmatrix} N^P_{\varepsilon_{xx}} & N^T_{\varepsilon_{xx}} \\ N^P_{\varepsilon_{zz}} & N^T_{\varepsilon_{zz}} \end{bmatrix}, \mathbf{N}_u(k,\omega) = \begin{bmatrix} N^P_{u_x} & N^T_{u_x} \\ N^P_{u_z} & N^T_{u_z} \end{bmatrix}.$$

The surface wavefield in the space-time domain can be obtained by applying the inverse two-dimensional Fourier transform. Using the residue calculus, the wavefield can be decomposed into individual mode waves:

$$\boldsymbol{\varepsilon}(x,t) = \frac{1}{2\pi} \int_{-\infty}^{+\infty} \sum_{\xi_n} \mathbf{H}_\varepsilon(\xi_n,\omega) \overline{\widetilde{\mathbf{F}}}(\xi_n,\omega) e^{i(\xi_n x + \omega t)} d\omega. \tag{3}$$

Here, the mode excitability $\mathbf{H}$ is derived from $\mathbf{N}$ and can be expressed as (see also **Equation A.3** in Appendix)

$$\mathbf{H}_\varepsilon(\xi_n,\omega) = \begin{bmatrix} H^P_{\varepsilon_{xx}} & H^T_{\varepsilon_{xx}} \\ H^P_{\varepsilon_{zz}} & H^T_{\varepsilon_{zz}} \end{bmatrix}.$$

NME can also be used to solve the excited wavefield as

$$\boldsymbol{\varepsilon}(x,t) = \frac{1}{2\pi} \int_{-\infty}^{+\infty} \sum_{\xi_n} i\xi_n \frac{\mathbf{u}_n|_{z=d} \mathbf{v}^*_n|_{z=d}}{4P_{nn}} \overline{\widetilde{\mathbf{F}}}(\xi_n,\omega) e^{i(\xi_n x + \omega t)} d\omega, \tag{4}$$

where P_{nn} is the power flow of mode n in x direction:

$$P_{nn} = \frac{1}{2} \int_{-d}^{+d} \left(-\mathbf{v}^*_n \boldsymbol{\sigma}_n \right) \vec{x} dz.$$

The superscript * denotes a complex conjugate. $\mathbf{v}_n = \begin{bmatrix} v_{n,z} & v_{n,x} \end{bmatrix}$ is the particle velocity of

mode n in z direction, and $\mathbf{u}_n = \begin{bmatrix} u_{n,x} & u_{n,z} \end{bmatrix}^T$ is the wave structure of the mode n in z

direction. The calculation of P_{nn} requires the stress tensor $\boldsymbol{\sigma}$ from **Equation A.1**. It should be

noted that **Equation 3** and **Equation 4** are mathematically equivalent. NME presents the

excitability function as the direction coupling between wave structure and loads which can

help better understand the influence of the coupling mechanism on different mode

excitability. On the other hand, MIT can present the excited wavefield in the k-ω domain

where the influence of source distribution of excitation loads can be easily treated as k and

ω filters on excitability function, which will be explained in the next section. The strain

wavefield is given as an example in **Equation 3** and **Equation 4**, and the displacement

wavefield can be obtained similarly from **Equation 2**.

2.1.2 Source distribution

The excitability function is determined by the coupling mechanism. The other term required

to calculate the wavefield is the load function $\mathbf{F}$. $\mathbf{F}$ can be separated into two independent

functions of distribution in space and time domains, respectively.

$$
\begin{aligned}
\mathbf{F}(x,t) &= \mathbf{h}(x)g(t) \\
\bar{\bar{\mathbf{F}}}(k,\omega) &= \tilde{\mathbf{h}}(k)\bar{g}(\omega)
\end{aligned}
\quad , \quad 0 \le x \le x_0, 0 \le t \le t_0 .
\tag{5}
$$

Time distribution g is related to applied voltage V, which is usually a Hanning-windowed

sinusoidal toneburst. Thus g can be expressed as

$$
g(t) = \frac{V_0}{2}\left(1 - \cos\left(\omega_0 t / N_C\right)\right)\sin\left(\omega_0 t\right)\left(\gamma(t) - \gamma(t - 2\pi N_C / \omega_0)\right) ,
\tag{6}
$$

where ω_0 is the center circular frequency, N_C is the cycle number of sinusoids, and γ

represents the Heaviside step function. Then the Fourier transform can be obtained as (see

also **Equation A.4** in Appendix)

$$
\bar{g}(\omega) = -\frac{i}{4}\left(\Lambda_1 + \Lambda_2 + \Lambda_3\right)V_0 .
\tag{7}
$$

Space distribution **h** is controlled by the tomography of printed electrodes. To simplify the problem, comb array electrodes of PCAT are discussed as illustrated in **Figure 2**. The excitation force can be determined by solving the actuator–plate coupled dynamic model. Due to the ignorable bonding layer, the shear stress T can be modelled as pin forces at the edge of each electrode element. T_0 is the unit stress per excitation voltage and is directly proportional to the piezoelectric constant d_{31} of PCAT ($T_0 \propto d_{31}$). Normal pressure P is modelled as even-distributed pressure within the electrode-covered range. P_0 is the unit pressure per excitation voltage and is directly proportional to the piezoelectric constant d_{33} of PCAT ($P_0 \propto d_{33}$). The piezopolymer coatings are polarized in the thickness direction. Thus $\mathbf{h}(x) = \begin{bmatrix} h_P(x) & h_T(x) \end{bmatrix}^T$ can be expressed as

Shear-stress model:

$$h_T(x) = \sum_{m=1}^{M_F^a} T_0 \left\{ \delta\left[x - (m-1)L_p^a - L_e^a \right] - \delta\left[x - (m-1)L_p^a \right] \right\}, \tag{8}$$

Normal-pressure model:

$$h_P(x) = \sum_{m=1}^{M_F^a} P_0 \left\{ \gamma\left[x - (m-1)L_p^a \right] - \gamma\left[x - (m-1)L_p^a - L_e^a \right] \right\}, \tag{9}$$

where L_e^a is the element length, L_p^a is the element pitch, $m = 1, 2, ... M_F^a$, M_F^a is the number of elements or comb fingers, and δ represents the Dirac Delta pulse function. Then, the Fourier transform can be obtained accordingly as

$$h_T(k) = T_0 \left(-2i \sin\left(k \frac{L_e^a}{2} \right) \right) \frac{\sin\left(k \frac{L_p^a}{2} M_F^a \right)}{\sin\left(k \frac{L_p^a}{2} \right)} e^{-ik\left(\frac{L_e^a}{2} + \frac{M_F^a - 1}{2} L_p^a \right)}, \tag{10}$$

and

$$h_P(k) = P_0 \left(\frac{2}{k} \sin\left(k\frac{L_e^a}{2} \right) \right) \frac{\sin\left(k\frac{L_p^a}{2} M_F^a \right)}{\sin\left(k\frac{L_p^a}{2} \right)} e^{-ik\left(\frac{L_e^a}{2} + \frac{M_F^a-1}{2}L_p^a \right)}. \tag{11}$$

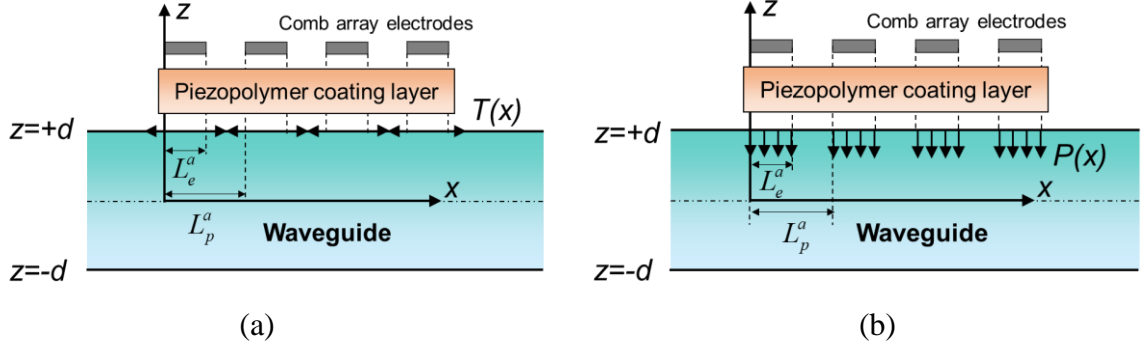(a)   (b)

Figure 2. Source distribution models of comb array electrodes: (a) shear-stress model under strain-coupling assumption; (b) normal-pressure model under displacement-coupling assumption.

2.1.3 Discussion of excitation mechanism

By substituting **Equation 10** and **Equation 11** into **Equation 5** and **Equation 2**, the excited wavefield in the *k-ω* domain can be obtained. The parameters as ω_0, N_C determine the tunability in the ω domain, and L_e^a, L_p^a, M_F^a are responsible for the tunability in the k domain. Thus, the $\bar{g}(\omega)$ and $\tilde{h}(k)$ in the load function can be treated as independent frequency and wavenumber filters applied to the excitability function. By applying the inverse two-dimensional Fourier transform as in **Equation 3**, the wavefield can be rewritten as

$$\boldsymbol{\varepsilon}(x,t) = \frac{1}{2\pi} \int_{-\infty}^{+\infty} \sum_{\xi_n} \mathbf{H}_\varepsilon(\xi_n, \omega) \begin{bmatrix} P_0 & 0 \\ 0 & T_0 \end{bmatrix} V_0 \mathbf{f}_k^a(\xi_n) f_\omega^a(\omega) e^{i\left[\xi_n\left(x - x_{center}^a \right) + \omega t \right]} d\omega, \tag{12}$$

where

13

$$\mathbf{f}_k^a\left(\xi_n\right)=\begin{bmatrix}f_{k,P}^a\left(\xi_n\right)\\f_{k,T}^a\left(\xi_n\right)\end{bmatrix}=\begin{bmatrix}\left(\dfrac{2}{\xi_n}\sin\left(\xi_n\dfrac{L_e^a}{2}\right)\right)\dfrac{\sin\left(\xi_n\dfrac{L_p^a}{2}M_F^a\right)}{\sin\left(\xi_n\dfrac{L_p^a}{2}\right)}\\[3em]\left(-2i\sin\left(\xi_n\dfrac{L_e^a}{2}\right)\right)\dfrac{\sin\left(\xi_n\dfrac{L_p^a}{2}M_F^a\right)}{\sin\left(\xi_n\dfrac{L_p^a}{2}\right)}\end{bmatrix}.$$

$$f_\omega^a\left(\omega\right)=-\frac{i}{4}\left(\Lambda_1+\Lambda_2+\Lambda_3\right)$$

$x_{center}^a=\left[L_e^a+\left(M_F^a-1\right)L_p^a\right]/2$ is the center location of the electrode-covered range which can be used to calculate the wave propagation distance as the actuator origin. By extracting the magnitude terms (P_0, T_0, V_0) from the load function, the dimensionless frequency and wavenumber filters or tuning functions of excitation for PCAT actuators can be obtained as $\mathbf{f}_k^a$ and f_ω^a. The flowchart is illustrated in **Figure 3**, where it can be observed that the excitation mechanism will influence the excitability function in the k-ω domain and the tuning function of excitation in the k domain.
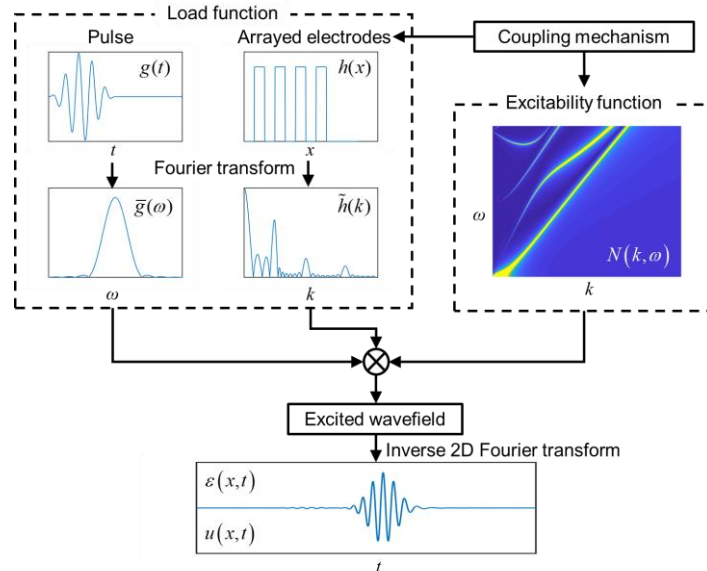

Figure 3. Flowchart of the analytical derivation of excited wavefield by PCAT actuators.

To determine the excitation mechanism of PCAT, the difference in excited wavefields

between strain-coupling (shear-stress) and displacement-coupling (normal-pressure) models needs to be discussed. The wavefield is firstly specified to be the out-of-plane displacement u_z, which can be easily measured by a commercial Laser vibrometer in experiments without worrying about the averaging effect from transducer sizes. The host waveguide is chosen to be an aluminum plate with a thickness of 2 mm. The corresponding mode excitability is then calculated and plotted in **Figure 4a** and **Figure 4b**. For both strain-coupling and displacement-coupling models, the excitability of A_0 mode shares a similar trend over frequencies. Out-of-plane displacement decreases rapidly from an asymptotically large value at low frequencies, and reaches a relatively stable value over the remaining frequency range. For the excitability of S_0 mode, however, distinct trends can be observed. For the strain-coupling model, the excitability of out-of-plane displacement is a flat curve over frequencies except around a rejecting point. For displacement-coupling model, out-of-plane displacement increases rapidly from an asymptotically small value at low frequencies to a plateau after reaching the peak value. The rejecting frequency for the strain-coupling model is about 1095 kHz, at which the wave structure of S_0 has a zero in-plane surface displacement (**Figure 4c**). According to **Equation 4**, the in-plane shear stress as the excitation force is decoupled with the wave structure on the surface at this frequency. Thus, it leads to the rejecting point on the excitability curve and the highly suppressed out-of-plane displacement wavefield.
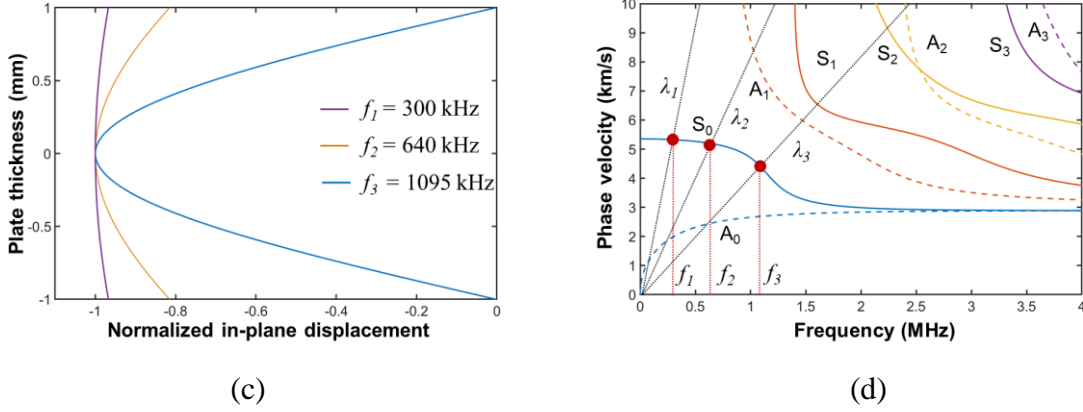

(a)   (b)

<div align="center">(c)</div>

<div align="center">(d)</div>
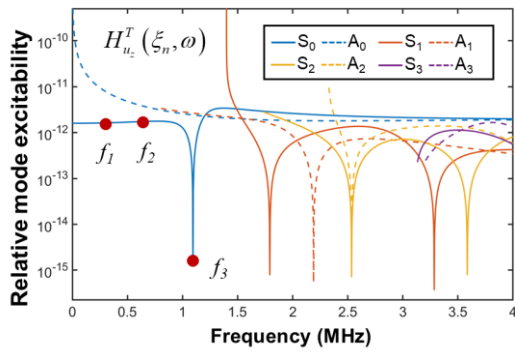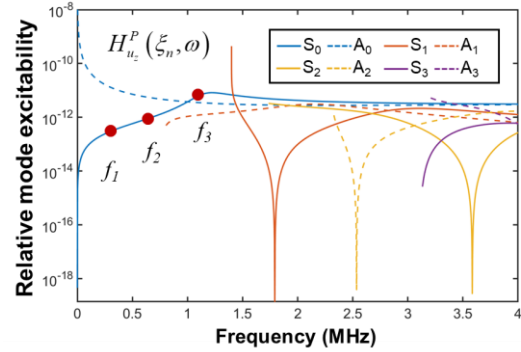
Figure 4. Relative mode excitability of out-of-plane displacement at various frequencies of (a) shear-stress model under strain-coupling assumption and (b) normal-pressure model under displacement-coupling assumption; (c) wave structures of in-plane displacement for S_0 at selected frequencies normalized by the maximum value; (d) phase velocity dispersion curves of the host aluminum plate.

According to the distinct behavior of S_0 mode excitability function on out-of-plane displacement wavefield, three frequencies (f_1, f_2, and f_3 in **Figure 4**) are selected to excite S_0 wave, from 300 kHz, 640 kHz, to the rejecting frequency of strain-coupling model at 1095 kHz. Their wavenumbers and wavelengths can be obtained from numerical results of the dispersion curves as in **Figure 4d**. Parameters of load function are set by *standard tuning*, i.e., $L_e^a = \lambda_{S_0}/2$ and $L_p^a = \lambda_{S_0}$. The number of comb fingers M_F^a is set to be four. The excitation signals of f_1 and f_2 are 5-cycle Hanning-windowed tonebursts. The cycle number of sinusoids N_C is increased to 10 for f_3 to compensate for the expansion of the bandwidth with increasing frequency. With these settings of parameters, the load function will have the peak value at the three selected frequencies of the S_0 mode. Thus, the difference in excited wavefields by different coupling mechanisms would be mainly attributed to the different mode excitability. The analytical results are shown in **Figure 6** with experimental results. Although not the focus of this study, there are also many other rejecting points of other modes in **Figure 4a** and **Figure 4b**, which are caused by either the decoupling between excitation forces and wave structures on the surface, or zero out-of-plane displacements of the wave structure itself.

<div align="center">16</div>

2.2. *Experimental verification*

2.2.1 Setups

The experimental setups were illustrated in **Figure 5**. The piezopolymer coatings were *in-situ* sprayed and functionalized on an aluminate plate of 350×350×2 mm following authors' previous work [22]. Three sets of comb array electrodes in *x* direction were printed on the coating layer with *standard tuning* by wavelengths of the three selected frequencies (λ_1, λ_2, and λ_3), respectively. The widths in *y* direction were uniform to be 60 mm to ensure plane wave propagation along *x* direction, corresponding to the plane strain assumption in analytical model. The inset in **Figure 5** is the calibration results of the piezoelectric constant d_{33} at their excitation frequencies by a dynamic measurement method, which verifies the non-resonance assumption in analytical models and is consistent with frequency sweep results in authors' previous work [22]. A signal generator and amplifier were used to apply high-voltage signals on thus-made PCAT actuators with a monitoring unit to calibrate the exact excitation voltage (~220 V_{pp}). A commercial laser vibrometer (Polytec PSV-400) was used to measure the out-of-plane displacement at 200 mm from the left edge of PCAT actuators with the help of retro-reflective tape. Damping clay was utilized to simulate low-reflecting boundary conditions around the plate for reducing interference in acquired signals from edge-reflected waves.
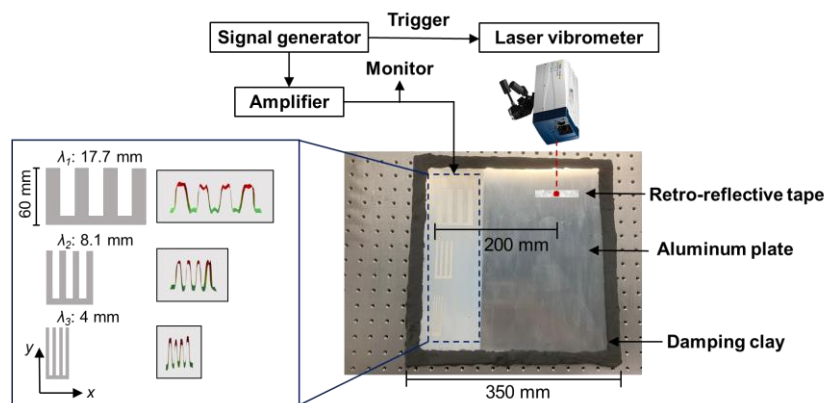

Figure 5. Experimental setups of PCAT actuators on an aluminum plate.

2.2.2 Results

As shown in **Figure 6**, the analytical results are consistent with the discussion in **Section 2.1.3**. The amplitude of the S_0 wave for the shear-stress model shows a dramatic decrease at f_3, while that for the normal-pressure model shows a steady increase from f_1, f_2 to f_3. The value is calculated by the envelope of S_0 wave packets and listed in **Table 1**. The waveform of S_0 at f_3 is distorted and split in the shear-stress model due to the rejection behavior. The obtained wave packets are formed by contribution from frequency components in the frequency bandwidth other than the rejecting point. The amplitude of the A_0 wave shares a similar trend in both analytical models as decreasing with frequencies. At f_1 and f_2, only two fundamental modes (S_0 and A_0) exist. At f_3, a high-order antisymmetric mode A_1 emerges, and S_0 wave arrives later than A_0 and A_1 waves, which is consistent with the calculated dispersion curves of group velocity (**Figure 7a**).

In experimental results, it is clear that the damping clay was successfully performed as low-reflecting boundaries, although not able to completely eliminate edge reflections. At f_1 and f_2, S_0 and A_0 wave packets can be clearly identified and separated due to the discrepancy in their wave velocities. At f_3, the overlap of waveforms can be observed due to the less discrepant wave velocities, which makes it difficult to identify A_0 and A_1 waves in a single-point measurement. To verify the existence of A_0 and A_1, two-dimensional Fourier transform was performed with a line scan over a 55 mm distance at a 0.5 mm step in an additional experiment. For convenience, the experimental results in the *k-ω* domain are plotted in the *f-1/λ* domain in **Figure 7b**, with the theoretical dispersion curves. The filtering effect by the tuning functions of wavenumber and frequency can be observed, which will be discussed in detail in the next section. The strongest energy distribution on the S_0 curve can be clearly observed around f_3, with weaker energy distribution on the A_1 curve and the weakest energy

distribution on the A_0 curve. These results are consistent with theoretical results and verify the simultaneous existence of S_0, A_0, and A_1 modes.

The amplitude of S_0 wave packets varying with frequencies in experimental results is calculated by the envelope and calibrated by piezoelectric constant d_{33} and excitation voltage in **Table 1**. It exhibits a steady increase and conforms more to the predicted trend by the normal-pressure model than by the shear-stress model. Therefore, it is reasonable to conclude that the excitation mechanism of PCAT actuators is mainly displacement coupling. However, the exact waveform is not the same between experimental results and the analytical normal-pressure model (*e.g.* relative mode amplitude S_0/A_0 in signals). The actual response may be a combination of strong displacement coupling and weak strain coupling, but it is difficult to determine the proportion due to many reasons. The pin-force and distributed-pressure excitation in analytical models represent highly idealized conditions. Although the experimental conditions were set to approach the assumptions in analytical models, spray and adhesion quality, property consistency, dimension error of electrodes, non-uniform source distribution on the coating layer, electrical/mechanical impedance and resonance, laser measurement error, and many other complex multi-physical phenomena possibly exist. The different excitation mechanism of PCATs from other surface-mounted actuators like PZTs and MFCs is probably mainly due to their low elastic modulus which is incomparable to the metal substrate. Therefore, their piezoelectric-induced strain cannot be effectively transferred as shear stress even by the strong lateral coupling.

It should be noted that, although the comb arrays are tuned by λ_{S_0}, A_0 wave still exists, and is even stronger than S_0 wave in the out-of-plane displacement at f_1. This is because of the joint effect of the mode excitability and source distribution of finite temporal pulse duration

and finite spatial electrode span. Thus, it is necessary to investigate a more comprehensive tuning method for mode control than the conventional *standard tuning* method which may not always be effective.
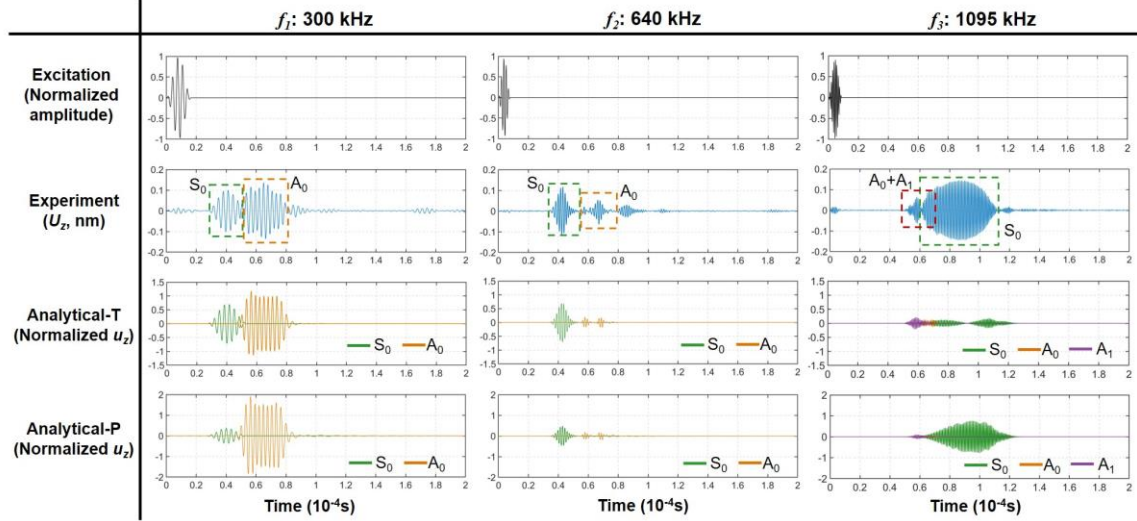

Figure 6. Excited wavefields of out-of-plane displacement by experiment, analytical shear-stress model (Analytical-T), and analytical normal-pressure model (Analytical-P) at three frequencies.

Table 1
Normalized amplitude of S_0 wave packets.

Group	f_1: 300 kHz	f_2: 640 kHz	f_3: 1095 kHz
Experiment	1	1.167	1.439
Experiment (calibrated)	1	1.244	1.449
Analytical-T	1	1.024	0.250
Analytical-P	1	1.332	2.086

(a)   (b)
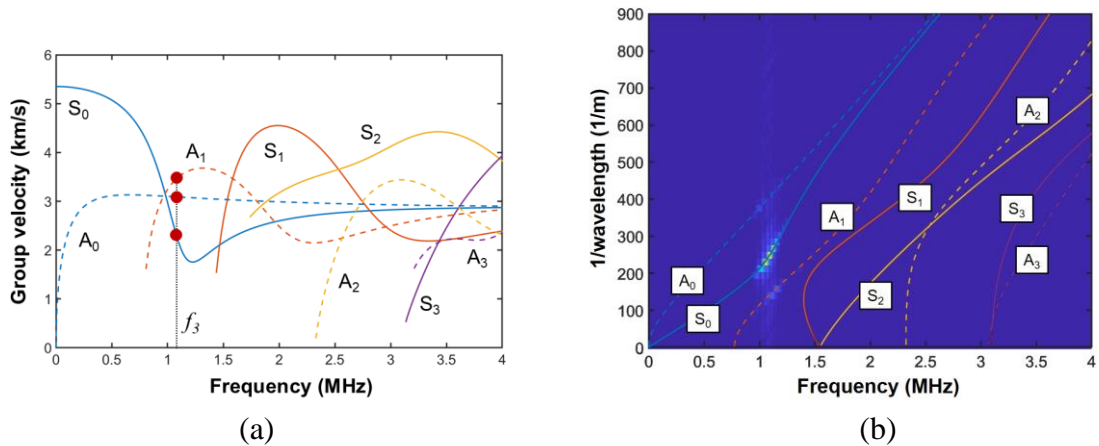
Figure 7. (a) Group velocity dispersion curves of the host plate; (b) experimental results of f_3 in k-f domain by two-dimensional Fourier transform.

2.3. Excitation tuning for mode control

20

2.3.1 Analytical solution

Since the excitation mechanism has been verified as mainly displacement coupling by analytical and experimental analysis, the normal-pressure model would be used for the discussion of excitation tuning for PCAT actuators henceforward. The most interested wavefields are surface in-plane strain ε_{xx} and out-of-plane displacement u_z, due to either strain-type or displacement-type measurement devices. The mode excitability $H_{\varepsilon_{xx}}^P$ and $H_{u_z}^P$ can be displayed as spectra on the dispersion curves (**Figure 8a** and **Figure 8b**) which indicate the strength of excited wave modes determined by the intrinsic coupling mechanism of PCAT actuators. According to **Equation 12**, the tuning functions of excitation $f_{k,P}^a$ and f_ω^a act as wavenumber and frequency filters on the excited wave modes in the *k-f* domain, which are determined by the source distribution of excitation force in space and time domains. They can be transformed as spectra in C_p-*f* domain, where intersected with dispersion curves. **Figure 9** is an example of the excitation tuning functions with parameter settings at *f₂* ($\omega_0 = 640$kHz and $N_C = 5$ of f_ω^a; $L_e^a = \lambda_2 / 2 = 4.05$mm, $L_p^a = \lambda_2 = 8.1$mm and $M_F^a = 4$ of $f_{k,P}^a$).
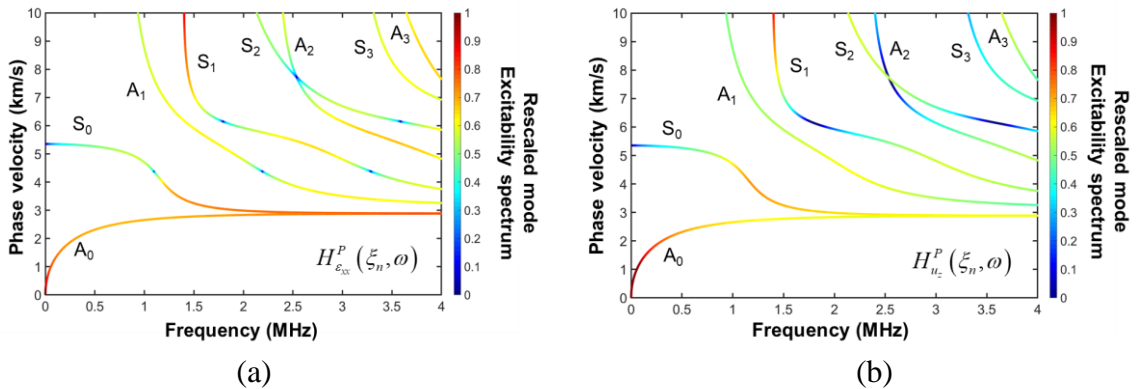

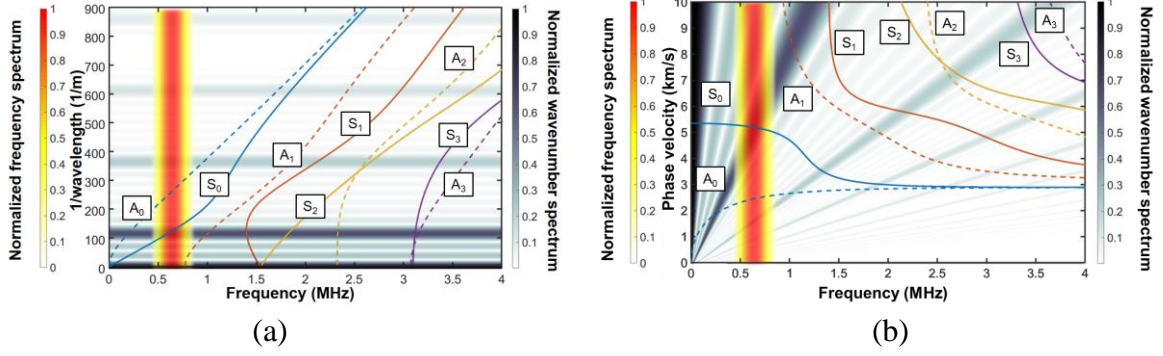**Figure 8.** Mode excitability spectra of (a) in-plane strain and (b) out-of-plane displacement.

Figure 9. The filtering spectra of tuning functions of excitation with parameter settings at f_2 intersected with dispersion curves in (a) k-f domain and (b) C_p-f domain.

The superposition of **Figure 8b** and **Figure 9** yields the excited wavefield of the analytical model at f_2 in **Figure 6**. It can be seen that the *standard tuning* method has a good mode control for S_0 at this frequency, which is also observed in the experimental results. However, for f_1 case, both the analytical and experimental results indicate poor mode control for S_0. From **Figure 8b** and **Figure 4b**, it can be seen that the mode excitability of S_0 is weakened when frequency decreases from f_2 to f_1, while the mode excitability of A_0 is strengthened. Such behavior of the mode excitability compromises the filtering effect by tuning functions of excitation and is unaltered due to the intrinsic excitation mechanism of PCAT. Thus, a more sophisticated tuning method needs to be further investigated to achieve better mode control, with the help of analytical solutions to tuning functions of excitation. The tuning functions of excitation for obtaining predominant S_0 wave at f_1 is discussed for example in the following.

Firstly, the tuning function of frequency f_ω^a is discussed. For a certain ω_0 with the increasing N_C, the peak value of f_ω^a at ω_0 will increase, while the width of the main lobe $4\omega_0 / N_C$ will decrease and the spread of frequency spectrum of the toneburst will be reduced. N_C is increased from 5, 7 to 10, and other settings are maintained for analytical analysis. **Figure 10** is the analytical wavefield of out-of-plane displacement. The amplitude of S_0

increases while the waveform of A_0 is distorted. Apparent elongation can be seen for both S_0 and A_0 waveforms which could result in an increasing degree of overlap of wave packets.
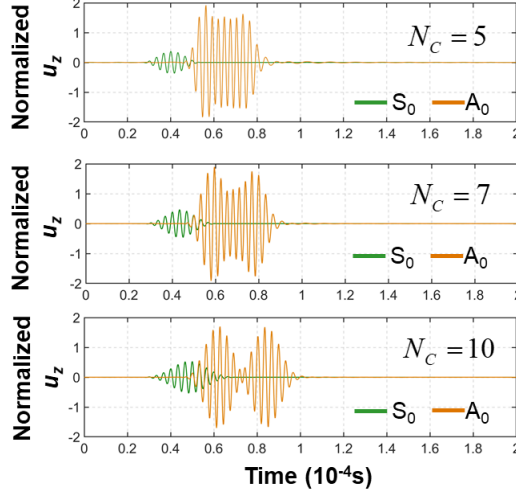

Figure 10. Analytical excitation of out-of-plane displacement wavefields at f_1 with increasing N_C.

The tuning function of wavenumber $f_{k,P}^a$ is then investigated. There are three parameters L_e^a, L_p^a and M_F^a distributed within two terms of $f_{k,P}^a$. The first term $\sin\left(\xi_n L_e^s/2\right)/\left(\xi_n/2\right)$ has peak value when $L_e^a = \dfrac{2n-1}{2}\lambda_{\xi_n}, L_e^a < L_p^a$. The second term $\sin\left(M_F^a \xi_n L_p^a/2\right)/\sin\left(\xi_n L_p^a/2\right)$ has peak values as M_F^a when $L_p^a = n\lambda_{\xi_n}$. Here n is an integer. With the *standard tuning* method when $n=1$ for both L_e^a and L_p^a , the value of $f_{k,P}^a$ has its maximum on the frequency-mode selections, but the distributions of $f_{k,P}^a$ on the other modes are also important to achieve mode control.

The element length L_e^a in the first term of $f_{k,P}^a$ is independent of the L_p^a and M_F^a in the second term. Thus L_e^a is first discussed with $L_p^a = \lambda_1$ and $M_F^a = 4$. Tuning functions $f_{k,P}^a\left(\xi_{(S_0,f_1)}\right)$ and $f_{k,P}^a\left(\xi_{(A_0,f_1)}\right)$ with varying L_e^a are plotted in **Figure 11**, where $\xi_{(S_0,f_1)}$ and

$\xi_{(A_0,f_1)}$ represent the wavenumber of S_0 and A_0 at f_1, respectively. Tuning functions appear to be periodic variations with L_e^a. As expected, $f_{k,P}^a\left(\xi_{(S_0,f_1)}\right)$ achieve its maximum when $L_e^a = \lambda_1/2$ and minimum when $L_e^a = \lambda_1$. Meanwhile, $f_{k,P}^a\left(\xi_{(A_0,f_1)}\right)$ has a near-peak value when $L_e^a = \lambda_1/2$. The multiplication of this value and the high excitability of A_0 at f_1 as in **Figure 8b** leads to the strong A_0 wave packets. On the other hand, even $f_{k,P}^a\left(\xi_{(S_0,f_1)}\right)$ is set to reach peak value by the *standard tuning* method, the low excitability of S_0 at f_1 is not sufficient to make it prevail over A_0 mode. The $f_{k,P}^a\left(\xi_{(A_0,f_1)}\right)$ curve has two rejecting points around $\lambda_1/2$, which is $\lambda_{(A_0,f_1)}$ and $2\lambda_{(A_0,f_1)}$. It can be expected that the high mode excitability of A_0 could be neutralized by the zero value of $f_{k,P}^a\left(\xi_{(A_0,f_1)}\right)$ at these points, although the value of $f_{k,P}^a\left(\xi_{(S_0,f_1)}\right)$ is biased from the peak value. Then L_e^a is biased to $\lambda_{(A_0,f_1)}$ for analytical analysis due to a relatively slight reduction of $f_{k,P}^a\left(\xi_{(S_0,f_1)}\right)$ value.

Figure 12 is the analytical wavefield of out-of-plane displacement. When $N_C = 5$, the amplitude of A_0 wave has been successfully reduced by half, although still stronger than S_0 wave. Theoretically, the amplitude of A_0 at f_1 should be zero, while the remaining A_0 wave packets are mainly components of the frequency bandwidth around f_1. N_C is again increased to 7 and 10. The amplitude of the S_0 wave is increased as in **Figure 10** by *standard tuning* while the suppression of A_0 becomes more effective. When N_C is increased to 10, S_0 wave prevails over A_0 wave. However, an increasing degree of overlap can be observed due to the elongation of the excitation signal. Thus, from the analysis of the theoretical model, *bias tuning* of L_e^a to match A_0 wavelength can achieve better mode control than *standard tuning*. Moreover, increasing N_C has a better effect of suppressing A_0 wave with *bias tuning* of L_e^a
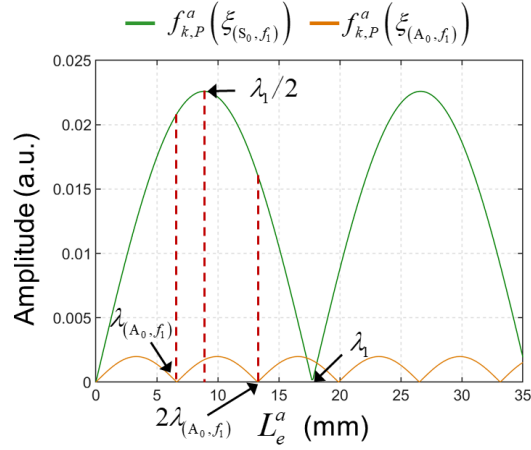
than merely distortion with *standard tuning*.

Figure 11. Tuning functions of (S_0, f_1) and (A_0, f_1) with varying element length.
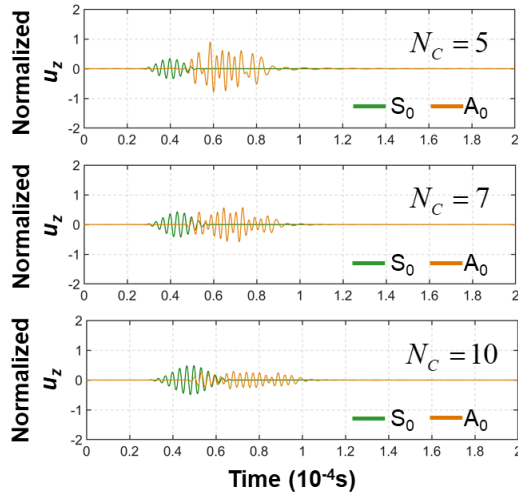

Figure 12. Analytical excitation of out-of-plane displacement wavefields at f_1 with increasing N_C by *bias tuning* of element length.

Next, the element pitch L_p^a and number of elements M_F^a is discussed with $L_e^a = \lambda_{(A_0, f_1)}$.

Variation of tuning function curves with L_p^a is more complicated than periodic variation with L_e^a, comprising of main lobes with high peak value and side lobes with low peak value.

The peak value of $f_{k,P}^a$ increases linearly with M_F^a. The rejecting points of zero value and bandwidth of lobes are determined by M_F^a. **Figure 13** is the $f_{k,P}^a$ curves when $M_F^a = 4$, where two rejecting points around λ_1 can be found, which is $2.5\lambda_{(A_0, f_1)}$ and $2.75\lambda_{(A_0, f_1)}$. To

achieve better mode control, L_p^a is biased to these two values and the analytical wavefields of out-of-plane displacement are plotted in **Figure 14**. The N_C is also increased from 5 to 7 and 10. The amplitude of the S_0 wave is increased with increasing N_C as expected and the suppression of A_0 is further improved. Interestingly, the performance of $L_p^a = 2.5\lambda_{(A_0,f_1)}$ is better than of $L_p^a = 2.75\lambda_{(A_0,f_1)}$, especially when N_C is 7 and 10. The reason is that $2.75\lambda_{(A_0,f_1)}$ is closer to the main lobe of $f_{k,P}^a\left(\xi_{(A_0,f_1)}\right)$ as shown in **Figure 13**. Components of the other frequencies within bandwidth around f_1 would benefit from the high value of the main lobe and contribute to A_0 wave packets, which compromise the suppression of A_0 wave at f_1. Thus, although $f_{k,P}^a\left(\xi_{(S_0,f_1)}\right)$ has a higher value at $2.75\lambda_{(A_0,f_1)}$ than $2.5\lambda_{(A_0,f_1)}$, the proper value of *bias tuning* of L_p^a is $2.5\lambda_{(A_0,f_1)}$ in this case.
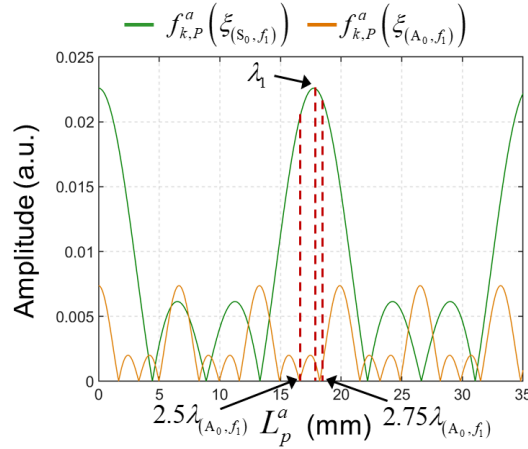

Figure 13. Tuning functions of (S_0, f_1) and (A_0, f_1) with varying element pitch.
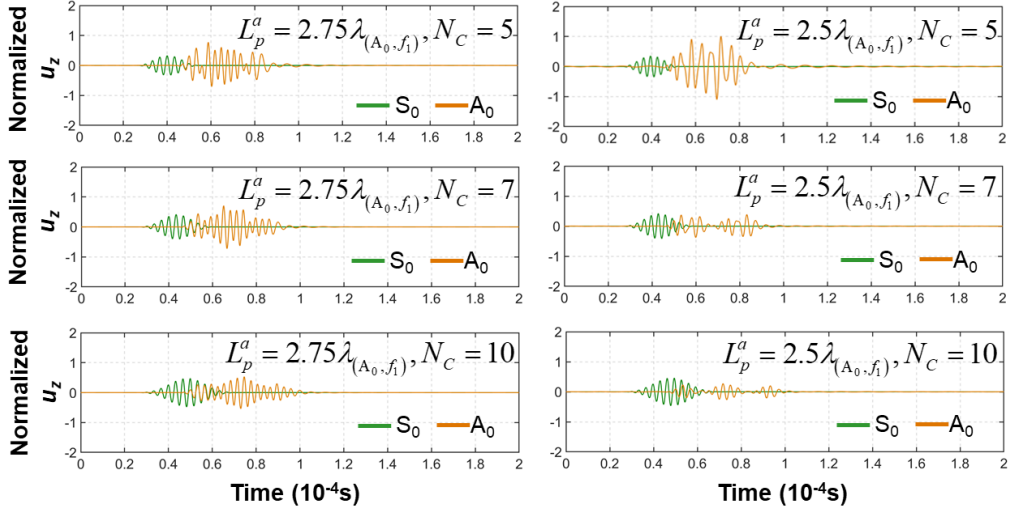
Figure 14. Analytical excitation of out-of-plane displacement wavefields at f_1 with increasing N_c by *bias tuning* of element pitch.

Similarly, for other M_F^a, the *bias tuning* of L_p^a can be found by plotting $f_{k,P}^a$ against L_p^a.

Analytical excited results are plotted in **Figure 15** with M_F^a increased from 1, 2, 3, 4, 6 to

8 and corresponding *bias tuning* of L_p^a. N_C is fixed to be 7. The corresponding excited

wavefields by *standard tuning* are shown in **Figure 16** for comparison. The consequent wave

amplitudes are measured in **Figure 17**. When $M_F^a = 1$ for a single element, there is no *bias*

tuning of L_p^a and the second term of tuning function is equal to 1. With increasing M_F^a, the

wave amplitude of S_0 increases as expected. For excited waveforms by *bias tuning*, the

amplitude of S_0 is only slightly reduced compared to the *standard tuning* case, while the

amplitude of A_0 is highly suppressed. When M_F^a is larger than 4, the S_0 wave becomes

stronger than A_0 wave. Similar to N_C, an increasing degree of overlap can be observed with

increasing M_F^a due to the elongation of excitation signals. Based on the analytical results,

the number of elements M_F^a is selected to be 4 for the following experimental studies,

considering the effect of mode control and overlap of wave packets. The amplitude ratio of

S_0/A_0 has been significantly improved from the original 0.24 by *standard tuning* to 1.15 by
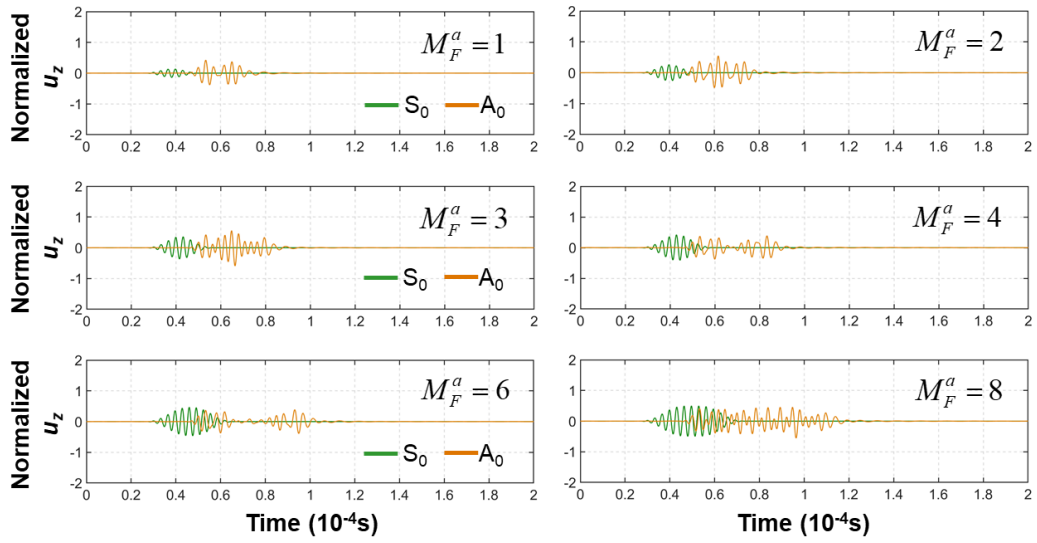
bias tuning.

Figure 15. Analytical excitation of out-of-plane displacement wavefield at f_1 with increasing number of elements and *bias tuning* of element length and pitch.
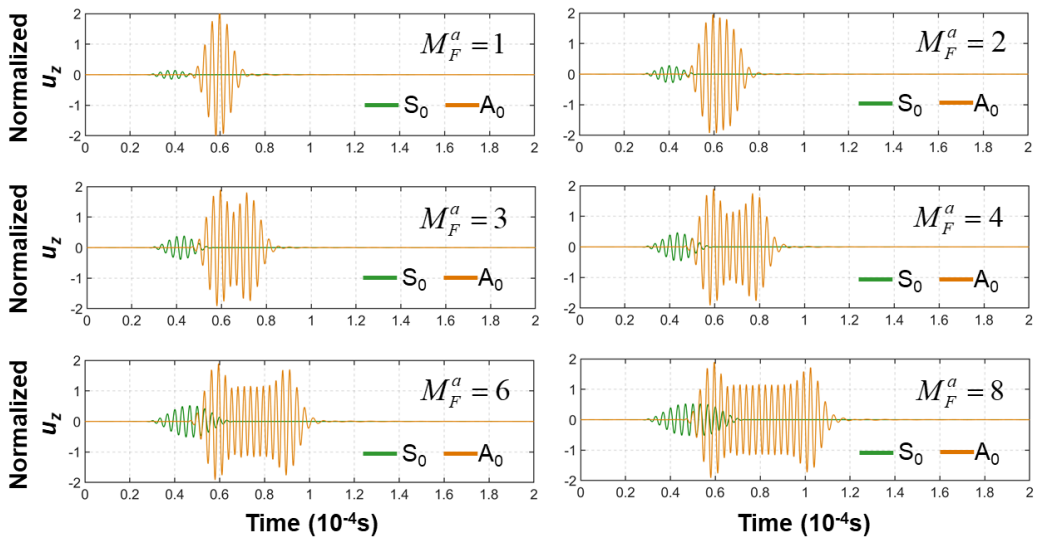

Figure 16. Analytical excitation of out-of-plane displacement wavefields at f_1 with increasing number of elements and *standard tuning* of element length and pitch.
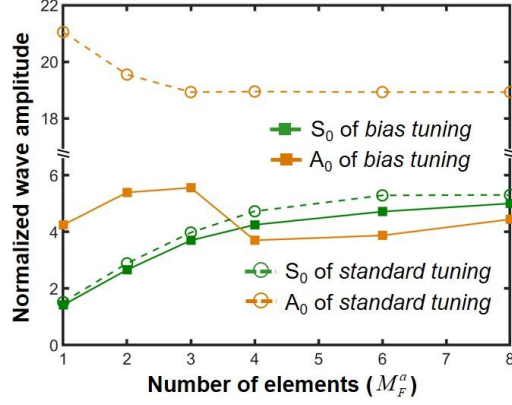
Figure 17. Normalized amplitudes of S_0 and A_0 wave with increasing number of elements of *standard tuning* and *bias tuning*.

2.3.2 Experimental verification

Experiments were conducted to verify the mode control by the *bias tuning* excitation method discussed above. Similar experimental setups of f_1 were applied as in **Section 2.2**. Element length and pitch were selected to be $\lambda_{(A_0, f_1)}$ and $2.5\lambda_{(A_0, f_1)}$ based on the analytical solutions. Number of elements was set to be 4. The cycle number of sinusoids in the Hanning-windowed excitation toneburst was firstly set to be 5, and increased to 7 and 10, conforming to analytical discussions. The measured out-of-plane displacements are shown in **Figure 18**. The experimental results show that the *bias tuning* excitation method is proven to achieve better mode control by effectively suppressing the undesired A_0 wave, compared with the original waveform in **Figure 6** by *standard tuning*. The amplitude of S_0 wave is only slightly decreased for $N_C = 5$ due to the bias of tuning functions from the peak value of S_0. Increasing N_C improves the mode control and also enhances the S_0 wave which is consistent with the predicted results of the theoretical model in **Figure 14**. When $N_C = 7$, S_0 wave appears predominant and the amplitude ratio of S_0/A_0 has been improved from 0.75 of *standard tuning* to 1.47 of *bias tuning*, although the suppression of A_0 wave is not further enhanced when N_C=10. The possible reason could be the error of printed electrode dimensions. It should be mentioned that the best solution for *bias tuning* excitation could

vary with different frequencies and modes. Nevertheless, the analytical discussion here is a fine example that can be followed for other cases.

In summary, for PCAT actuators, the mode waveforms in Lamb-wave excitation are controlled by filtering effects of excitation tuning functions in frequency and wavenumber domains. Suppression of a certain mode can be achieved by finding the rejecting points of element length and pitch, although a side effect is the diminishment of the main mode due to *bias tuning*. Prolonging the excitation pulse duration and increasing number of elements could enhance the main mode and improve the suppression of other modes by narrowing the bandwidths in frequency and wavenumber domains respectively, although the consequent overlap of wave packets needs to be concerned.
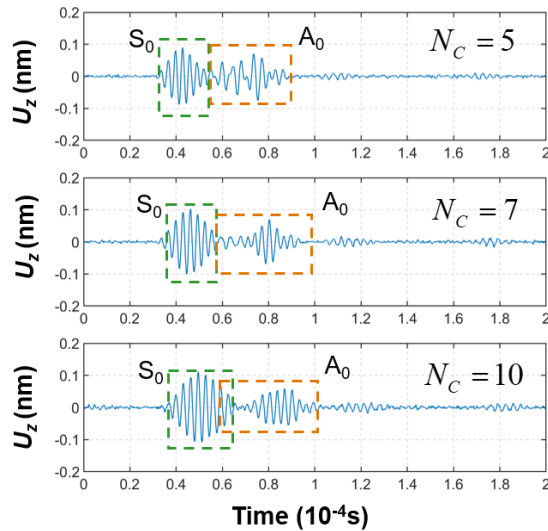

Figure 18. Excitation of out-of-plane displacement wavefields by experimental measurement at f_1 with increasing N_c by *bias tuning* of element length and pitch.

3. Lamb-wave Acquisition by PCAT Sensors

3.1. Analytical model

Next, Lamb-wave acquisition is investigated by PCAT sensors. Since PCAT is of thin thickness and low stiffness, the sensors would not alter the incident wave and experience the

same wavefield as the host structure. Thus, the essential behavior of sensors can be treated as the averaging of wavefields passing through the spatial electrode span of the sensor-covered area [15-17]. As shown in **Figure 19**, the comb array electrode pattern of sensors (with element length L_e^s, pitch L_p^s, and number M_F^s) is discussed as in the analytical model of actuators. Both types of coupling mechanisms are considered to develop the analytical model of acquisition. Under plane strain assumption, the response voltage can be expressed as

$$V = \frac{D \sum_{m=1}^{M_F^s} \left(\int_{x_m^s - L_e^s/2}^{x_m^s + L_e^s/2} U(x,t)\, dx \right)}{M_F^s L_e^s}, \tag{13}$$

$$x_m^s = x_1 + (m-1) L_p^s, \quad m = 1, 2, \ldots M_F^s$$

where x_1 is the center of the first comb element. U is the incident wavefield and D is the transfer coefficient that can be solved by piezoelectric equations. The term $1/M_F^s L_e^s$ represents the spatial averaging effect over the PCAT electrode-covered area, which also holds for conventional Lamb wave sensors. When the sensor-covered area tends to zero, *e.g.* using a laser vibrometer, the sensor response tends to a quantity proportional to the local strain. When the sensor-covered area increases, the general trend is a monotonic decrease in the output voltage, as a result of averaging the strain wavefield over the sensor-covered area. For strain coupling, the waveform response is in-plane strain and D is directly proportional to the piezoelectric constant g_{31} of PCAT ($D_S \propto g_{31}$). For displacement coupling, the waveform response is out-of-plane displacement and D is directly proportional to the piezoelectric constant g_{33} of PCAT ($D_D \propto g_{33}$).
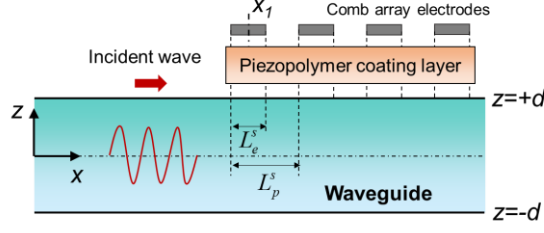
Figure 19. Analytical model of PCAT sensor on a metal waveguide.

3.1.1. Arbitrary wavefield

Arbitrary wavefield can be transformed with MIT as

$$U(x,t) = \frac{1}{4\pi^2} \int_{-\infty}^{+\infty}\int_{-\infty}^{+\infty} \bar{\bar{U}}(k,\omega) e^{i(kx+\omega t)} dk d\omega .$$ (14)

According to the orthogonality of Lamb wave modes or residue calculus, the wavefield is the superposition of mode components as

$$U(x,t) = \frac{1}{2\pi} \sum_{\xi_n} \int_{-\infty}^{+\infty} U'(\xi_n,\omega) e^{i(\xi_n x+\omega t)} d\omega .$$ (15)

Substituting **Equation 15** into **Equation 13**:

$$V = \frac{D}{2\pi} \sum_{\xi_n} \int_{-\infty}^{+\infty} U'(\xi_n,\omega) f_k^s(\xi_n) e^{i(\xi_n x_{center}^s + \omega t)} d\omega,$$ (16)

where

$$f_k^s(\xi_n) = \frac{\sin(\xi_n L_e^s / 2)}{\xi_n L_e^s / 2} \frac{\sin(M_F^s \xi_n L_p^s / 2)}{M_F^s \sin(\xi_n L_p^s / 2)}.$$

$x_{center}^s = x_0 + (M_F^s - 1) L_p^s / 2$ is the center location of the electrode-covered range which can be used to calculate the wave propagation distance as the sensor origin. The influence of the spatial distribution of comb arrays can be treated as a *k* filter on the incident wavefield. The dimensionless filter or tuning function of acquisition for PCAT sensors can be represented as f_k^s. It should be noted that different from Lamb-wave excitation, there is no frequency filter in Lamb-wave acquisition and the tuning function is the same for both strain and

32

displacement models.

3.1.2. PCAT-excited wavefield

It is generally difficult to obtain the actual wavefield in **Equation 16** by experiments. In this study, PCAT actuators have been proven to be displacement-type with analytical results of excited wavefields in **Equation 12**. Substituting into **Equation 13**, the waveform response can be obtained when PCATs are used for actuators and sensors in SHM, like networks. Take the strain-coupling model for example:

$$V = \frac{DP_0V_0}{2\pi} \sum_{\xi_n} \int_{-\infty}^{+\infty} H_{\varepsilon_{xx}}^P \left(\xi_n, \omega\right) f_\omega^a \left(\omega\right) f_{k,P}^a \left(\xi_n\right) f_k^s \left(\xi_n\right) e^{i\left(\xi_n\left(x_{center}^s - x_{center}^a\right) + \omega t\right)} d\omega. \qquad \textbf{(17)}$$

The response of the displacement-coupling model can be obtained similarly by substituting PCAT-excited wavefields of out-of-plane displacement. According to **Figure 4c**, the surface in-plane strain of S_0 is nearly zero at f_3. Thus the corresponding S_0 mode excitability has a rejecting point of in-plane strain as shown in **Figure 8a**, which is quite different from the excitability of normal displacement in **Figure 8b**. To determine the acquisition mechanism of PCAT sensors, the waveform response of PCAT sensors to PCAT-excited wavefield is calculated, at f_1, f_2, and f_3. The *standard tuning* method is used with the same electrode patterns for both actuators and sensors. The other settings are the same as in **Section 2**. The analytical results are shown in **Figure 21** with experimental results.

3.2. Experimental verification

3.2.1 Setups

The experimental setups of actuators were the same as in **Section 2.2.1**. For sensors, the width in y direction were uniform to be 20 mm to ensure plane wave acquisition. The element length and pitch were the same as actuators. The response of sensors were amplified before
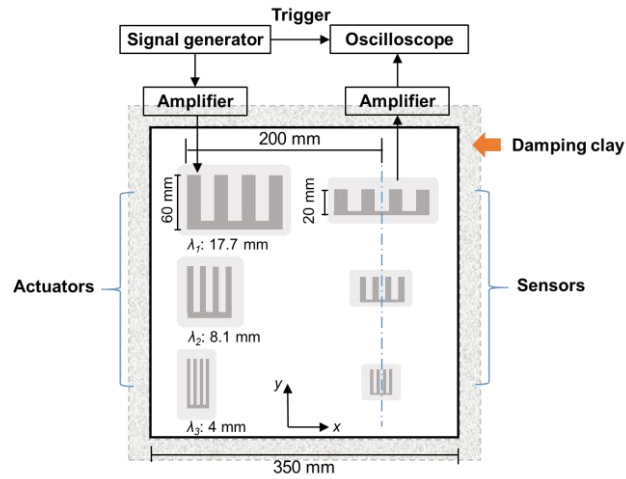
transmitting to an oscilloscope (**Figure 20**).

Figure 20. Experimental setups of PCAT sensors on an aluminum plate (the dimensions of PCAT are exaggerated for clear illustration).

3.2.2 Results

For the displacement-coupling model, the S_0 wave response of PCAT sensors increases from f_1, f_2, to f_3, but the values are lower than the original excited out-of-plane displacement captured by a single point in **Figure 6**. This is due to the spatial averaging effect of the tuning function, which will be discussed in detail in the next section. Another influence of the tuning function is the suppression of undesired other modes. With the wavenumber filter of acquisition, mode control has been improved, and A_0/A_1 waves are almost eliminated in response of out-of-plane displacement at f_2 and f_3. However, at f_1, A_0 wave is still stronger than S_0 wave, and overlap can be observed which has not happened in the original PCAT-excited wavefield. This is due to the covered range of PCAT sensors with multiple fingers, which will be discussed in detail in the next section. For the strain-coupling model, the response of S_0 is almost the same at f_1 and f_2, but is highly neutralized by the zero value of the rejecting point at f_3 as expected.

In experimental results, the amplitude of A_0 wave packets is decreased with increasing

frequency. At f_3, a weak and long waveform is detected, which is the overlap of A_0, A_1, and S_0. The experimental response of PCAT sensors to PCAT-excited wavefields is in accordance with the trend of the strain-coupling model. Thus it is reasonable to conclude that the acquisition mechanism of PCAT sensors is mainly strain type, which is different from the verified displacement type of PCAT actuators.
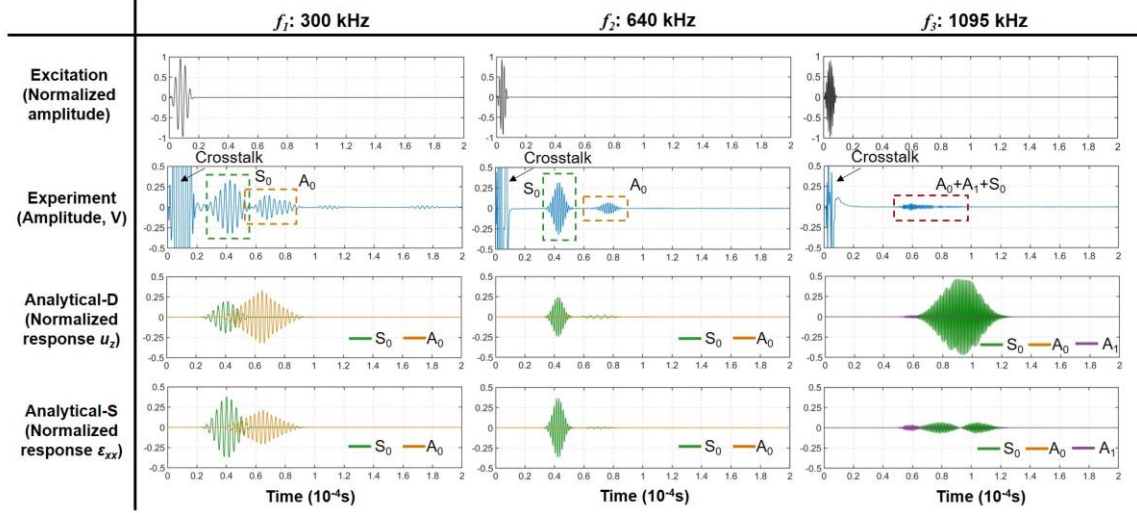

Figure 21. Acquisition of PCAT-excited wavefields by experiment, analytical displacement-coupling model (Analytical-D), and analytical strain-coupling model (Analytical-S) at three frequencies.

3.3. *Acquisition tuning for mode control*

3.3.1 Analytical solution

Since the acquisition mechanism has been verified as mainly strain coupling by analytical and experimental analysis, the in-plane strain response would be used for the discussion of acquisition tuning for PCAT sensors henceforward. To investigate the tunability of PCAT sensors, the PCAT-excited wavefield at f_1 by the *standard tuning* excitation method with poor mode control is used as the original wavefield. The *standard tuning* acquisition method refers to using the same configuration of actuators to design sensors. The parameter study of the tuning function of acquisition f_k^s is similar to the wavenumber tuning function of excitation $f_{k,P}^a$, due to their similar form. There are also three parameters L_e^s, L_p^s, and M_F^s

35

distributed within two terms of f_k^s. The element length L_e^s in the first term $\sin\left(\xi_n L_e^s / 2\right)/\left(\xi_n L_e^s / 2\right)$ is independent of the L_p^s and M_F^s in the second term $\sin\left(M_F^s \xi_n L_p^s / 2\right)/M_F^s \sin\left(\xi_n L_p^s / 2\right)$. Thus L_e^s is first discussed with $L_p^s = \lambda_1$ and $M_F^s = 4$. As plotted in **Figure 22**, f_k^s has its maximum value as 1 when L_e^s is approximating to zero, which is corresponding to the original wavefield captured by a single point. The peak value decreases and the minimum value is obtained when $L_e^s = n\lambda_{\xi_n}, L_e^s < L_p^s$. Here n is an integer. This is the spatial averaging effect of L_e^s. To achieve better mode control, L_e^s is biased from the *standard tuning* value $\lambda_1/2$ to $\lambda_{(A_0,f_1)}$. The acquisition results are plotted in **Figure 23**. The *bias tuning* acquisition method has better performance of mode control than the *standard tuning* method as expected, and the S$_0$ wave is stronger, although still smaller than the original wavefield due to the spatial averaging effect of L_e^s. Further reducing L_e^s could increase the wave amplitude, but would be detrimental to the suppression of other wave modes (as $\lambda_{(A_0,f_1)}/2$ in **Figure 23**).
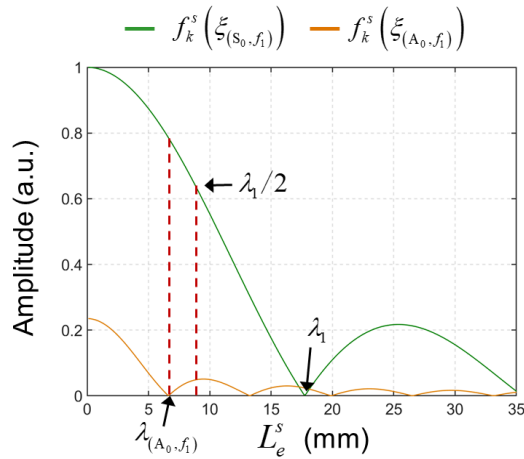

Figure 22. Acquisition tuning functions of (S$_0$, f_1) and (A$_0$, f_1) with varying element length.
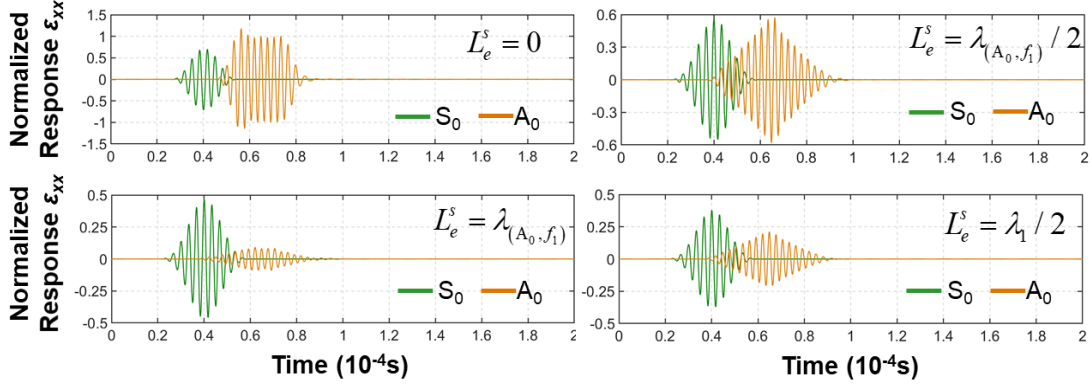
Figure 23. Analytical acquisition of in-plane strain wavefields at f_1 with varying element length.

Next, the element pitch L_p^s and number of elements M_F^s are discussed with $L_e^s = \lambda_{(A_0, f_1)}$. f_k^s

has the same form as $f_{k,P}^a$, except that the peak value is not increased with increasing M_F^s.

Taking $M_F^s = 4$ as an example, the curve of f_k^s is similar to $f_{k,P}^a$ in **Figure 13** with the same

biased value $2.5\lambda_{(A_0, f_1)}$ of L_p^s. Similarly, the *bias tuning* of L_p^s can be found for other values

of M_F^s by plotting f_k^s against L_p^s, *e.g.* $L_p^s = 2\frac{1}{3}\lambda_{(A_0, f_1)}$ for $M_F^s = 3$. Analytical acquisition

results are plotted in **Figure 24** with M_F^s increased from 1, 2, 3, 4, 6 to 8 and corresponding

bias tuning of L_p^s. The corresponding acquisition results by *standard tuning* are shown

Figure 25 for comparison. The consequent wave amplitudes are measured in **Figure 26**.

Similar to L_p^a of actuators, there is no *bias tuning* of L_p^s of sensors when $M_F^s = 1$, since the

second term of tuning function is equal to 1 of a single element. The *bias tuning* method has

again overwhelmed the *standard tuning* method. The amplitude of the S$_0$ wave is the joint

effect of enhancement by decreased L_e^s and reduction by biased L_p^s. The mode control has

been greatly improved with better suppression of the A$_0$ wave. It should be noted that the

standard tuning method also has a certain degree of mode controlling of the original

wavefield due to the filtering effect. However, the wave amplitudes of S$_0$ and A$_0$ decrease

with increasing M_F^s. The reason is that although the peak value is the same with varied M_F^s, narrowing of bandwidth would decrease the overall energy of wave packets. Moreover, besides N_C and M_F^a of actuators, M_F^s of sensors would further elongate the captured waveforms which cause more serious overlap. It can also be seen that the mode control is generally improved with increasing M_F^s, and the best performance can be achieved with *bias tuning* of L_p^s when $M_F^s = 6$. Considering mode control, wave amplitude, and overlap of wave packets, $M_F^s = 3$ is selected for the proper PCAT sensors in this study with *bias tuning* of L_p^s to $2\frac{1}{3}\lambda_{(A_0,f_1)}$. The amplitude ratio of S0/A0 has been significantly improved from 0.7 of the original wavefield and 1.7 by *standard tuning* to 5.6 by *bias tuning*.
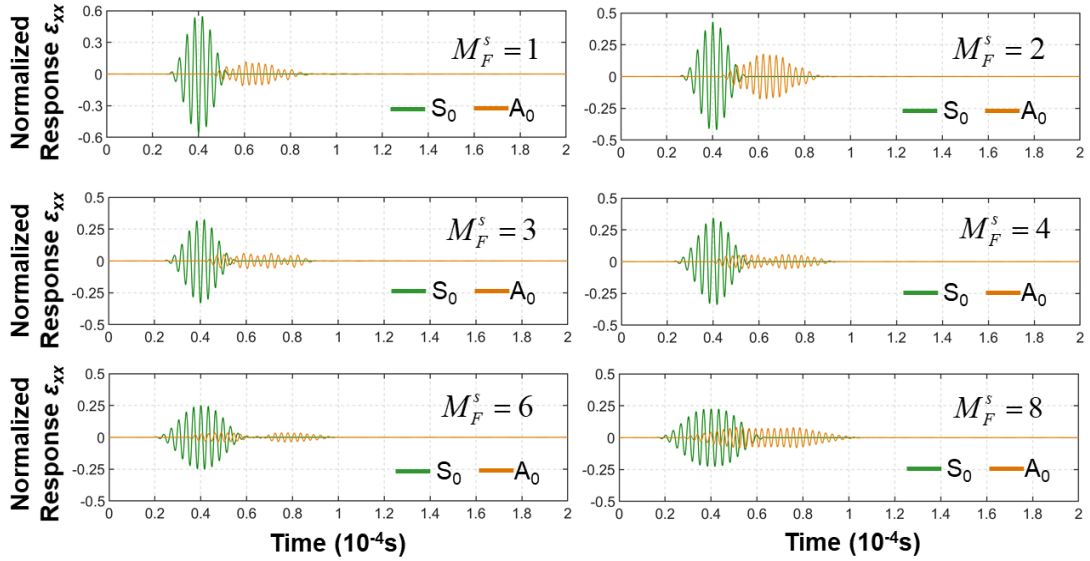

Figure 24. Analytical acquisition of in-plane strain wavefields at f_1 with varying number of elements and *bias tuning* of element length and pitch.
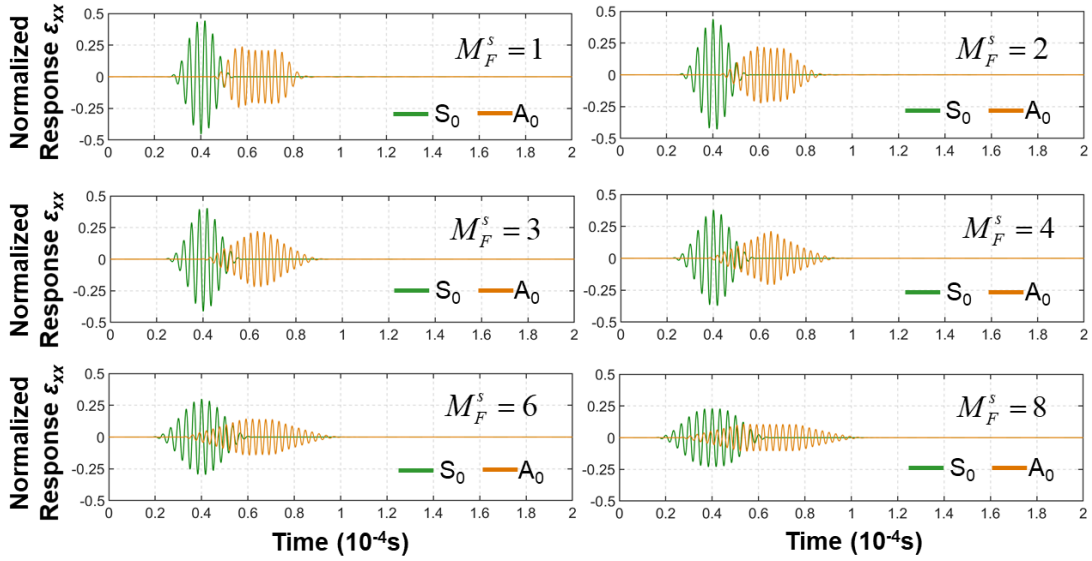
Figure 25. Analytical acquisition of in-plane strain wavefields at f_1 with varying number of elements and *standard tuning* of element length and pitch.
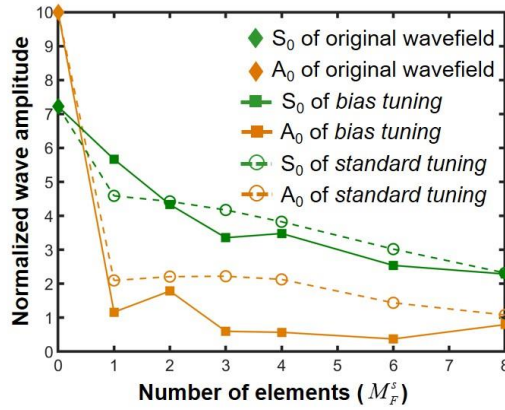

Figure 26. Normalized amplitudes of S_0 and A_0 wave with increasing number of elements of *standard tuning* and corresponding *bias tuning*.

3.3.2 Experimental verification

Experiments were conducted to verify the mode control by the *bias tuning* acquisition method discussed above. Similar experimental setups of f_1 were applied as in **Section 3.2**. The parameters of the actuator remained the same. The cycle number of sinusoids in the Hanning-windowed excitation toneburst was set to be 5. For the sensors, three *bias tuning* cases were studied with parameters listed in **Table 2**. *bias tuning* 2 and 3 correspond to

$M_F^s = 1$ and $M_F^s = 3$ in **Figure 24**. The element length of a single-element sensor is further reduced to 2 mm in *bias tuning* 1. The experimental response is shown in **Figure 27**. Compared with the results of *standard tuning* in **Figure 21**, the number of cycles in the waveforms is smaller when number of elements is decreased to 1 and 3, which verifies the elongation effect of number of elements. The amplitudes of S_0 and A_0 is measured and plotted in **Figure 28**. *Bias tuning* 3 has the best performance of suppressing A_0 wave and the amplitude ratio of S_0/A_0 has been improved from 2 of *standard tuning* to 2.87 of *bias tuning*, although not as good as in analytical results. The possible reasons are summarized in the following aspects: (a) some properties of actuators and sensors are not considered in the simplified and ideal analytical models under assumptions made in **Section 2.1**, which could also contribute to the experimental results, including lateral dimension, electrode layer, impedance, and resonance; (b) the incident waves experience scattering and attenuation when propagating on the plate which are not considered in analytical solutions; (c) the manufacturing error could affect the consistency of piezoelectricity across the function layer and accuracy of printed electrodes in locations, dimensions, and angles, which could also influence the incident wavefields. These issues could cause deviation of bandwidth of incident waves from the theoretical rejecting point and thus leading to compromised performance of *bias tuning* in experiments. They also indicate the inadequacy of the plane strain models used for analytical solutions of incident waves excited by actuators and output response of sensors. For SHM applications on plate-like structures, two-dimensional tuning models, the scattering of excited waves, and sensing directivity should be further investigated for PCAT-based networks. Nevertheless, the analytical discussion here is a fine example that can be followed. Further reduction of element length in *bias tuning* 1 could increase the amplitude of S_0 wave, however, the amplitude of A_0 wave is also increased with poor mode control. Such phenomenon is also consistent with analytical discussions.

Table 2
Parameter settings in different groups.

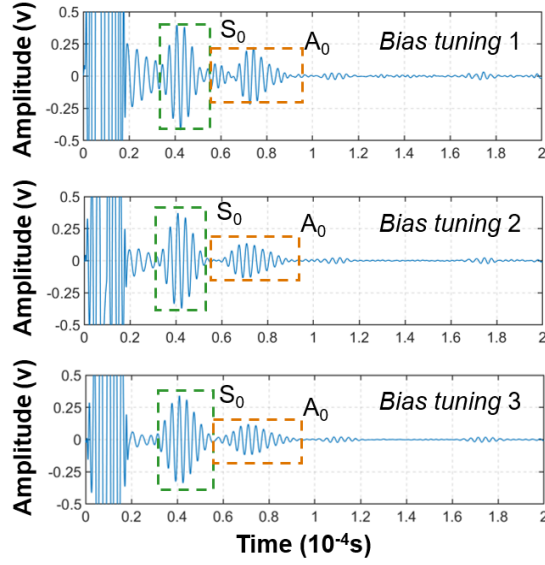| Group	Element length (mm)	Element pitch (mm)	Number of elements
Bias tuning 1	2	N/A	1
Bias tuning 2	6.63 ($\lambda_{(A_0,f_1)}$)	N/A	1
Bias tuning 3	6.63 ($\lambda_{(A_0,f_1)}$)	15.5 ($2\frac{1}{3}\lambda_{(A_0,f_1)}$)	3
Standard tuning	8.85 ($\lambda_1/2$)	17.7 (λ_1)	4

Figure 27. Experimental response of PCAT sensors to PCAT-excited wavefields at f_1 by *bias tuning* of element length and pitch.
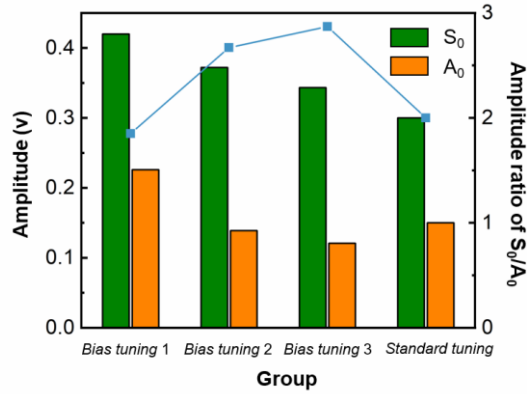

Figure 28. Amplitude of S_0 and A_0 wave packets in different groups.

In summary, for PCAT sensors, the mode waveforms in Lamb-wave acquisition are controlled by the filtering effect of acquisition tuning functions in the wavenumber domain. Suppression of a certain mode can be achieved by finding the rejecting points of element

41

length and pitch. The main mode could be enhanced by *bias tuning* of element length to a lower value and be diminished by *bias tuning* of element pitch. Increasing number of elements could improve the suppression of other modes by narrowing the bandwidth in the wavenumber domain, but also cause the diminishment of the main mode due to the decreasing overall energy of wave packets. The overlap of wave packets is another side effect of increasing number of elements of PCAT sensors.

4. Perspectives of Inter-digital Electrodes and Polarization Direction

In this study, comb array electrodes were used for PCAT actuators and sensors, with the function layer vertical polarized. In many studies, Inter-digital electrodes of two comb arrays were also tried for PVDF or MFC transducers. In some cases, the piezoelectric layer was still vertical polarized. A bottom ground electrode layer was required and a bipolar voltage source was used to excite two comb arrays out-of-phase [30, 31, 36-38]. The analytical wavefield can be obtained by modifying the analytical model in this study with load directions of comb arrays reversed each other. In other cases, the piezoelectric layer was lateral polarized [39-41], although authors still doubt the effectiveness of laterally polarizing the thin piezopolymer layer. The bottom ground electrode layer was not necessary and the functional area in the analytical model needs to be changed to the inter-finger area. For strain-type actuators as MFC, excited wavefields can be strengthened by taking advantage of stronger d_{33} rather than d_{31} to transfer shear stress with lateral polarization. On the contrary, for displacement-type actuators as PCAT or PVDF, excited wavefields can be weakened due to the reduced normal pressure by d_{31} with lateral polarization. On the other hand, PCAT or PVDF is strain-type sensor like MFC. Thus, the acquisition of wavefields could also benefit from the stronger g_{33} than g_{31} with later polarization by inter-digital electrodes. Thus, appropriate polarization directions must be chosen to avoid adverse effects for PCAT.

5. Concluding Remarks

In this study, distinctly different excitation and acquisition mechanisms of PCAT are revealed by analytical and experimental analysis. It should be noted that such a difference does not contradict elastodynamic reciprocity conditions. The tunability of PCAT is studied with analytical solutions. The corresponding *bias tuning* methods are proposed and verified by experiments. PCAT actuators are of displacement type, which is different from other *in-situ* fixed transducers. The conventional *standard tuning* excitation method could achieve the largest amplitude of the desired mode. However, the undesired modes cannot be effectively controlled in some cases due to mode excitability, *e.g.* A_0 wave in the low-frequency range. To achieve better mode control, the rejecting points of tuning functions of undesired modes are found to bias the element length and pitch. Increasing the cycle number of excitation tonebursts and number of elements could further enhance the desired mode and improve the filtering effect of *bias tuning* to suppress undesired modes, but with inevitable elongation of waveforms that could cause overlap. PCAT sensors are of strain type, which is the same as other *in-situ* fixed transducers. The same parameters as *standard tuning* of excitation could obtain neither a strong response of the desired mode nor good mode control in some cases, due to the spatial averaging effect. The acquisition tuning behavior is investigated. Better mode control could be achieved with *bias tuning*. Increasing number of elements would further elongate the acquired waveforms. For PCAT actuators and sensors, the best solutions of the multi-parameter *bias tuning* for mode control in Lamb-wave excitation and acquisition require to be investigated case by case.

Without losing generality, plane-wave assumption and comb array electrodes are used in this study for convenience. The method could be further extended to circular-crested waves by arc-shape actuators, angular acquisition of rectangle-shape sensors, and inter-digital

electrodes. In this study, the *bias tuning* method is discussed in the low-frequency range, where only two fundamental modes exist. For mode control in the high-frequency range, a synthetic consideration of multi-mode suppression is required. The methodology of investigation in this study can also be extended to other types of monolithic or arrayed Lamb-wave transducers.

The results demonstrate the critical role played by the dimensions and the coupling mechanisms of PCAT for Lamb-wave excitation and acquisition. The coupling mechanism needs to be considered when selecting particular frequency-mode excitation and acquisition for damage detection. The proposed *bias tuning* method can be used to design specific actuators and sensors with good mode control of predominant desired mode and suppressed undesired modes, which could greatly benefit the signal processing in Lamb wave-based SHM. This work sheds light on the development of PCAT-based networks for Lamb wave-based SHM. Several issues are to be resolved in authors' future work, including two-dimensional models for tuning actuators and sensors, omnidirectional excitation of circular-crested waves, and sensing directivity of angled incident waves. Moreover, the applications to damage detection with fine-tuned network layouts in real engineering structures are also under investigation.

Appendix

The Lamb wave structure across the thickness:

44

$$u_x^S = -2i\xi_S^2 q\cos(qd)\cos(pz) + iq(\xi_S^2 - q^2)\cos(pd)\cos(qz)$$

$$u_z^S = 2\xi_S pq\cos(qd)\sin(pz) + \xi_S(\xi_S^2 - q^2)\cos(pd)\sin(qz)$$

$$u_x^A = 2i\xi_A^2 q\sin(qd)\sin(pz) - iq(\xi_A^2 - q^2)\sin(pd)\sin(qz)$$

$$u_z^A = 2\xi_A pq\sin(qd)\cos(pz) + \xi_A(\xi_A^2 - q^2)\sin(pd)\cos(qz)$$

$$\sigma_{xx}^S = 2\mu\xi_S q\left[(\xi_S^2 + q^2 - 2p^2)\cos(qd)\cos(pz) - (\xi_S^2 - q^2)\cos(pd)\cos(qz)\right]$$

$$\sigma_{zz}^S = -2\mu\xi_S q(\xi_S^2 - q^2)\left[\cos(qd)\cos(pz) - \cos(pd)\cos(qz)\right] \qquad , \qquad \textbf{(A.1)}$$

$$\sigma_{xz}^S = i\mu\left[4\xi_S^2 pq\cos(qd)\sin(pz) + (\xi_S^2 - q^2)^2\cos(pd)\sin(qz)\right]$$

$$\sigma_{xx}^A = -2\mu\xi_A q\left[(\xi_A^2 + q^2 - 2p^2)\sin(qd)\sin(pz) - (\xi_A^2 - q^2)\sin(pd)\sin(qz)\right]$$

$$\sigma_{zz}^A = -2\mu\xi_A q(\xi_A^2 - q^2)\left[\sin(qd)\sin(pz) - \sin(pd)\sin(qz)\right]$$

$$\sigma_{xz}^A = i\mu\left[4\xi_A^2 pq\sin(qd)\cos(pz) + (\xi_A^2 - q^2)^2\sin(pd)\cos(qz)\right]$$

where μ is the shear modulus. Superscript S represents symmetric modes and A for antisymmetric modes.

The matrix components of excitability function:

$$N_{\varepsilon_{xx}}^P = \frac{1}{2\mu}\left(\begin{array}{c} \dfrac{-k^2(k^2-q^2)\sin(pd)\cos(qd) - 2k^2 pq\cos(pd)\sin(qd)}{D_A} \\ +\dfrac{-k^2(k^2-q^2)\cos(pd)\sin(qd) - 2k^2 pq\sin(pd)\cos(qd)}{D_S} \end{array}\right)$$

$$N_{\varepsilon_{zz}}^P = \frac{1}{2\mu}\left(\dfrac{-ikp(k^2+q^2)\cos(pd)\cos(qd)}{D_A} + \dfrac{ikp(k^2+q^2)\sin(pd)\sin(qd)}{D_S}\right)$$

$$N_{\varepsilon_{xx}}^T = \frac{1}{2i\mu}\left(\dfrac{-kq(k^2+q^2)\sin(pd)\sin(qd)}{D_A} + \dfrac{kq(k^2+q^2)\cos(pd)\cos(qd)}{D_S}\right) \qquad , \qquad \textbf{(A.2)}$$

$$N_{\varepsilon_{zz}}^T = \frac{1}{2i\mu}\left(\begin{array}{c} \dfrac{ik^2(k^2-q^2)\sin(pd)\cos(qd) + 2ik^2 pq\cos(pd)\sin(qd)}{D_A} \\ +\dfrac{ik^2(k^2-q^2)\cos(pd)\sin(qd) + 2ik^2 pq\sin(pd)\cos(qd)}{D_S} \end{array}\right)$$

where

$$D_S = (k^2-q^2)^2\cos(pd)\sin(qd) + 4k^2 pq\sin(pd)\cos(qd)$$
$$D_A = (k^2-q^2)^2\sin(pd)\cos(qd) + 4k^2 pq\cos(pd)\sin(qd) \quad .$$

The matrix components of mode excitability function:

$$H^P_{\varepsilon_{xx}} = \frac{i}{2\mu}\left(\begin{array}{c} \dfrac{-\xi_A^{\,2}(\xi_A^{\,2}-q^2)\sin(pd)\cos(qd)-2\xi_A^{\,2}pq\cos(pd)\sin(qd)}{D'_A(\xi_A)} \\[2mm] +\dfrac{-\xi_S^{\,2}(\xi_S^{\,2}-q^2)\cos(pd)\sin(qd)-2\xi_S^{\,2}pq\sin(pd)\cos(qd)}{D'_S(\xi_S)} \end{array}\right)$$

$$H^P_{\varepsilon_{zz}} = \frac{i}{2\mu}\left(\dfrac{-i\xi_A p(k^2+q^2)\cos(pd)\cos(qd)}{D'_A(\xi_A)}+\dfrac{i\xi_S p(k^2+q^2)\sin(pd)\sin(qd)}{D'_S(\xi_S)}\right),\quad \textbf{(A.3)}$$

$$H^T_{\varepsilon_{xx}} = \frac{1}{2\mu}\left(\dfrac{-\xi_A q(\xi_A^{\,2}+q^2)\sin(pd)\sin(qd)}{D'_A(\xi_A)}+\dfrac{\xi_S q(\xi_S^{\,2}+q^2)\cos(pd)\cos(qd)}{D'_S(\xi_S)}\right)$$

$$H^T_{\varepsilon_{zz}} = \frac{1}{2\mu}\left(\begin{array}{c} \dfrac{i\xi_A^{\,2}(\xi_A^{\,2}-q^2)\sin(pd)\cos(qd)+2i\xi_A^{\,2}pq\cos(pd)\sin(qd)}{D'_A(\xi_A)} \\[2mm] +\dfrac{i\xi_S^{\,2}(\xi_S^{\,2}-q^2)\cos(pd)\sin(qd)+2i\xi_S^{\,2}pq\sin(pd)\cos(qd)}{D'_S(\xi_S)} \end{array}\right)$$

where

$$D'_S = \partial D_S / \partial k$$
$$D'_A = \partial D_A / \partial k \,.$$

The components of Fourier transform of a Hanning-windowed sinusoidal toneburst:

$$\Lambda_1 = \frac{2\pi N_C}{\omega_0}\left\{ \mathrm{sinc}\left(\frac{\pi N_C}{\omega_0}(\omega-\omega_0)\right)e^{-i\frac{\pi N_C}{\omega_0}(\omega-\omega_0)} - \mathrm{sinc}\left(\frac{\pi N_C}{\omega_0}(\omega+\omega_0)\right)e^{-i\frac{\pi N_C}{\omega_0}(\omega+\omega_0)} \right\}$$

$$\Lambda_2 = -\frac{\pi N_C}{\omega_0}\left\{ \begin{array}{l} \mathrm{sinc}\left(\frac{\pi N_C}{\omega_0}\left(\omega-\frac{N_C-1}{N_C}\omega_0\right)\right)e^{-i\frac{\pi N_C}{\omega_0}\left(\omega-\frac{N_C-1}{N_C}\omega_0\right)} \\[2mm] -\mathrm{sinc}\left(\frac{\pi N_C}{\omega_0}\left(\omega+\frac{N_C+1}{N_C}\omega_0\right)\right)e^{-i\frac{\pi N_C}{\omega_0}\left(\omega+\frac{N_C+1}{N_C}\omega_0\right)} \end{array} \right\}$$

$$\Lambda_3 = -\frac{\pi N_C}{\omega_0}\left\{ \begin{array}{l} \mathrm{sinc}\left(\frac{\pi N_C}{\omega_0}\left(\omega-\frac{N_C+1}{N_C}\omega_0\right)\right)e^{-i\frac{\pi N_C}{\omega_0}\left(\omega-\frac{N_C+1}{N_C}\omega_0\right)} \\[2mm] -\mathrm{sinc}\left(\frac{\pi N_C}{\omega_0}\left(\omega+\frac{N_C-1}{N_C}\omega_0\right)\right)e^{-i\frac{\pi N_C}{\omega_0}\left(\omega+\frac{N_C-1}{N_C}\omega_0\right)} \end{array} \right\}\,. \quad \textbf{(A.4)}$$

CRediT authorship contribution statement

Yehai Li: Conceptualization, Methodology, Data curation, Formal analysis, Investigation, Validation, Visualization, Writing - original draft. **Kai Wang**: Methodology, Investigation, Validation, Writing - review & editing. **Wei Feng**: Project administration, Writing - review & editing. **Hefeng Wu**: Investigation. **Zhongqing Su**: Validation, Writing - review & editing. **Shifeng Guo**: Project administration, Supervision, Writing - review & editing, Funding acquisition.

Declaration of Competing Interest

The authors declare that they have no known competing financial interests or personal relationships that could have appeared to influence the work reported in this paper.

Acknowledgments

References

[1] Z. Su, L. Ye, Identification of damage using Lamb waves: from fundamentals to applications, Springer Science & Business Media, 2009.

[2] V.K. Chillara, C.J. Lissenden, Review of nonlinear ultrasonic guided wave nondestructive evaluation: theory, numerics, and experiments, Opt. Eng. , 55 (2015) 011002. https://doi.org/10.1117/1.Oe.55.1.011002

[3] K. Wang, Y. Li, Z. Su, R. Guan, Y. Lu, S. Yuan, Nonlinear aspects of "breathing" crack-disturbed plate waves: 3-D analytical modeling with experimental validation, Int. J. Mech. Sci. , 159 (2019)

140-150. https://doi.org/10.1016/j.ijmecsci.2019.05.036

[4] C. Younho, Estimation of ultrasonic guided wave mode conversion in a plate with thickness variation, IEEE Trans. Ultrason. Ferroelectr. Freq. Control, 47 (2000) 591-603. https://doi.org/10.1109/58.842046

[5] C. Zhang, Z. Zhang, H. Ji, J. Qiu, C. Tao, Mode conversion behavior of guided wave in glass fiber reinforced polymer with fatigue damage accumulation, Compos. Sci. Technol. , 192 (2020) 108073. https://doi.org/10.1016/j.compscitech.2020.108073

[6] S.H.K. Reddy, A. Vasudevan, P. Rajagopal, K. Balasubramaniam, Scattering of Higher Order Mode Clusters (HOMC) from surface breaking notches in plates with application to higher temperature gradients, NDT&E Int., 120 (2021) 102441. https://doi.org/10.1016/j.ndteint.2021.102441

[7] Ł. Ambroziński, T. Stepinski, Robust polarization filter for separation of Lamb wave modes acquired using a 3D laser vibrometer, Mech. Syst. Signal Pr., 93 (2017) 368-378. https://doi.org/10.1016/j.ymssp.2017.02.002

[8] P. Khalili, P. Cawley, Excitation of Single-Mode Lamb Waves at High-Frequency-Thickness Products, IEEE Trans. Ultrason. Ferroelectr. Freq. Control, 63 (2016) 303-312. https://doi.org/10.1109/TUFFC.2015.2507443

[9] J. Li, J.L. Rose, Implementing guided wave mode control by use of a phased transducer array, IEEE Trans. Ultrason. Ferroelectr. Freq. Control, 48 (2001) 761-768. https://doi.org/10.1109/58.920708

[10] G. Veit, P. Bélanger, An ultrasonic guided wave excitation method at constant phase velocity using ultrasonic phased array probes, Ultrasonics, 102 (2020) 106039. https://doi.org/10.1016/j.ultras.2019.106039

[11] Y. Wang, L. Qiu, Y. Luo, R. Ding, F. Jiang, A piezoelectric sensor network with shared signal transmission wires for structural health monitoring of aircraft smart skin, Mech. Syst. Signal Pr., 141 (2020) 106730. https://doi.org/10.1016/j.ymssp.2020.106730

[12] P. Li, S. Shan, F. Wen, L. Cheng, A fully-coupled dynamic model for the fundamental shear horizontal wave generation in a PZT activated SHM system, Mech. Syst. Signal Pr., 116 (2019) 916-932. https://doi.org/10.1016/j.ymssp.2018.07.010

[13] M. Mańka, M. Rosiek, A. Martowicz, T. Stepinski, T. Uhl, PZT based tunable Interdigital Transducer for Lamb waves based NDT and SHM, Mech. Syst. Signal Pr., 78 (2016) 71-83. https://doi.org/10.1016/j.ymssp.2015.12.013

[14] V. Giurgiutiu, Structural Health Monitoring with Piezoelectric Wafer Active Sensors, 2nd ed., Academic Press, 2014.

[15] A. Raghavan, C.E.S. Cesnik, Modeling of piezoelectric-based Lamb-wave generation and sensing for structural health monitoring, P Soc Photo-Opt Ins, 5391 (2004) 419-430. https://doi.org/10.1117/12.540269

[16] F. Lanza di Scalea, H. Matt, I. Bartoli, The response of rectangular piezoelectric sensors to Rayleigh and Lamb ultrasonic waves, The Journal of the Acoustical Society of America, 121 (2007) 175-187. https://doi.org/10.1121/1.2400668

[17] C. Hakoda, V.K. Chillara, C. Pantea, The effect of a transducer's spatial averaging on an elastodynamic guided wave's wavenumber spectrum, Ultrasonics, 114 (2021) 106422. https://doi.org/10.1016/j.ultras.2021.106422

[18] X. Lin, F.G. Yuan, Diagnostic Lamb waves in an integrated piezoelectric sensor/actuator plate: analytical and experimental studies, Smart Mater. Struct., 10 (2001) 907-913. https://doi.org/10.1088/0964-1726/10/5/307

[19] Z. Wenhao, J.L. Rose, Lamb wave generation and reception with time-delay periodic linear arrays: a BEM simulation and experimental study, IEEE Trans. Ultrason. Ferroelectr. Freq. Control, 46 (1999) 654-664. https://doi.org/10.1109/58.764852

[20] J. Jin, S.T. Quek, Q. Wang, Analytical solution of excitation of Lamb waves in plates by inter-digital transducers, P Roy Soc a-Math Phy, 459 (2003) 1117-1134. https://doi.org/10.1098/rspa.2002.1071

[21] E.V. Glushkov, N.V. Glushkova, W. Seemann, O.V. Kvasha, Elastic wave excitation in a layer by piezoceramic patch actuators, Acoust. Phys. , 52 (2006) 398-407. https://doi.org/10.1134/S106377100604004X

[22] Y. Li, W. Feng, L. Meng, K.M. Tse, Z. Li, L. Huang, Z. Su, S. Guo, Investigation on in-situ sprayed, annealed and corona poled PVDF-TrFE coatings for guided wave-based structural health monitoring: From crystallization to piezoelectricity, Materials & Design, 199 (2021) 109415. https://doi.org/10.1016/j.matdes.2020.109415

[23] Y. Wang, S. Hu, T. Xiong, Y. Huang, L. Qiu, Recent progress in aircraft smart skin for structural health monitoring, Struct. Health Monit., (2021) 14759217211056831. https://doi.org/10.1177/14759217211056831

[24] H. Gu, M.L. Wang, A Monolithic Interdigitated PVDF Transducer for Lamb Wave Inspection, Struct Health Monit, 8 (2009) 137-148. https://doi.org/10.1177/1475921708102104

[25] B. Ren, C.J. Lissenden, PVDF Multielement Lamb Wave Sensor for Structural Health Monitoring, IEEE Trans. Ultrason. Ferroelectr. Freq. Control, 63 (2016) 178-185. https://doi.org/10.1109/TUFFC.2015.2496423

[26] Y. Zhu, X. Zeng, M. Deng, K. Han, D. Gao, Detection of nonlinear Lamb wave using a PVDF comb transducer, NDT&E Int., 93 (2018) 110-116. https://doi.org/10.1016/j.ndteint.2017.09.012

[27] V.T. Rathod, G. Raju, L. Udpa, S. Udpa, Y. Deng, Multimode guided wave extraction capabilities using embedded thin film sensors in a composite laminated beam, Sens. Actuators, A 309 (2020) 112040. https://doi.org/10.1016/j.sna.2020.112040

[28] B. Lin, V. Giurgiutiu, Modeling and testing of PZT and PVDF piezoelectric wafer active sensors, Smart Mater. Struct., 15 (2006) 1085-1093. https://doi.org/10.1088/0964-1726/15/4/022

[29] E.V. Glushkov, N.V. Glushkova, O.V. Kvasha, R. Lammering, Selective Lamb mode excitation by piezoelectric coaxial ring actuators, Smart Mater. Struct., 19 (2010) 035018. https://doi.org/10.1088/0964-1726/19/3/035018

[30] R.S.C. Monkhouse, P.D. Wilcox, P. Cawley, Flexible interdigital PVDF transducers for the generation of Lamb waves in structures, Ultrasonics, 35 (1997) 489-498. https://doi.org/10.1016/S0041-624X(97)00070-X

[31] J.P. Koduru, J.L. Rose, Transducer arrays for omnidirectional guided wave mode control in plate like structures, Smart Mater. Struct., 22 (2012) 015010. https://doi.org/10.1088/0964-1726/22/1/015010

[32] H. Kim, F. Torres, Y. Wu, D. Villagran, Y. Lin, T.-L. Tseng, Integrated 3D printing and corona poling process of PVDF piezoelectric films for pressure sensor application, Smart Mater. Struct., 26 (2017) 085027. https://doi.org/10.1088/1361-665x/aa738e

[33] T. Siponkoski, M. Nelo, H. Jantunen, J. Juuti, A printable P(VDF-TrFE)-PZT Composite with Very High Piezoelectric Coefficient, Appl. Mater. Today, 20 (2020) 100696. https://doi.org/10.1016/j.apmt.2020.100696

[34] M. Philibert, S. Chen, V.-K. Wong, W.H. Liew, K. Yao, C. Soutis, M. Gresil, Direct-write piezoelectric coating transducers in combination with discrete ceramic transducer and laser pulse excitation for ultrasonic impact damage detection on composite plates, Struct. Health Monit., (2021) 14759217211040719. https://doi.org/10.1177/14759217211040719

[35] J.L. Rose, Ultrasonic guided waves in solid media, Cambridge university press, 2014.

[36] P.D. Wilcox, P. Cawley, M.J.S. Lowe, Acoustic fields from PVDF interdigital transducers, Iee P-sci Meas Tech, 145 (1998) 250-259. https://doi.org/10.1049/ip-smt:19982213

[37] T. Liu, M. Veidt, S. Kitipornchai, Single mode Lamb waves in composite laminated plates generated by piezoelectric transducers, Compos. Struct., 58 (2002) 381-396. https://doi.org/10.1016/S0263-8223(02)00191-5

[38] J. Jin, S.T. Quek, Q. Wang, Design of interdigital transducers for crack detection in plates, Ultrasonics, 43 (2005) 481-493. https://doi.org/10.1016/j.ultras.2004.09.005

[39] Y. Lugovtsova, A. Bulletti, P. Giannelli, L. Capineri, J. Prager, Characterization of a Flexible Piezopolymer-based Interdigital Transducer for Selective Excitation of Ultrasonic Guided Waves, 2020 IEEE International Ultrasonics Symposium (IUS), (2020) 1-4. https://doi.org/10.1109/IUS46767.2020.9251702

[40] V. Rathod, D. Roy Mahapatra, Ultrasonic guided wave sensing properties of PVDF thin film with inter digital electrodes, SPIE Smart Structures and Materials + Nondestructive Evaluation and Health Monitoring, 9062 (2014). https://doi.org/10.1117/12.2047314

[41] A.V. Mamishev, K. Sundara-Rajan, Y. Fumin, D. Yanqing, M. Zahn, Interdigital sensors and transducers, Proc. IEEE 92 (2004) 808-845. https://doi.org/10.1109/JPROC.2004.826603